# WHAMM functions in kidney reabsorption and polymerizes actin to promote autophagosomal membrane closure and cargo sequestration

Alyssa M. Coulter[a,†], Valerie Cortés[b,†], Corey J. Theodore[a], Rachel E. Cianciolo[c], Ron Korstanje[b,*], and Kenneth G. Campellone[a,d,*]

[a]Department of Molecular & Cell Biology, Institute for Systems Genomics, University of Connecticut, Storrs, CT 06269; [b]The Jackson Laboratory, Bar Harbor, ME 04609; [c]Niche Diagnostics LLC, Columbus, OH 43201; [d]Center on Aging, UConn Health, Farmington, CT 06030

**ABSTRACT** **The actin cytoskeleton is essential for many functions of eukaryotic cells, but the factors that nucleate actin assembly are not well understood at the organismal level or in the context of disease. To explore the function of the actin nucleation factor WHAMM in mice, we examined how *Whamm* inactivation impacts kidney physiology and cellular proteostasis. We show that male WHAMM knockout mice excrete elevated levels of albumin, glucose, phosphate, and amino acids, and display structural abnormalities of the kidney proximal tubule, suggesting that WHAMM activity is important for nutrient reabsorption. In kidney tissue, the loss of WHAMM results in the accumulation of the lipidated autophagosomal membrane protein LC3, indicating an alteration in autophagy. In mouse fibroblasts and human proximal tubule cells, WHAMM and its binding partner the Arp2/3 complex control autophagic membrane closure and cargo receptor recruitment. These results reveal a role for WHAMM-mediated actin assembly in maintaining kidney function and promoting proper autophagosome membrane remodeling.**

**Monitoring Editor**
Terry Lechler
Duke University

Received: Jan 22, 2024
Revised: Apr 1, 2024
Accepted: Apr 5, 2024

New Hypothesis

New Materials

## SIGNIFICANCE STATEMENT

- The tissue-specific functions of mammalian actin nucleation factors are not well understood.
- Mice lacking the actin nucleation factor WHAMM show signs of a kidney disease resembling Fanconi Syndrome. Kidneys from WHAMM-deficient male mice display abnormalities in structure and reabsorption function. Cultured proximal tubule cells exhibit defects in autophagosome closure and autophagic cargo sequestration.
- WHAMM and the Arp2/3 complex are important for nutrient reabsorption in the kidney and autophagosome remodeling in proximal tubule cells.

This article was published online ahead of print in MBoC in Press (http://www.molbiolcell.org/cgi/doi/10.1091/mbc.E24-01-0025) on April 10, 2024.

†These authors contributed equally to this work.

*Address correspondence to: Ron Korstanje (ron.korstanje@jax.org); Kenneth G Campellone (kenneth.campellone@uconn.edu).

Abbreviations used: Arp2/3, Actin-related protein 2/3; GABARAP, GABA type A receptor-associated protein; GMS, Galloway-Mowat Syndrome; LC3, microtubule-associated protein 1 light chain 3; STX17, Syntaxin-17; WASP, Wiskott-Aldrich Syndrome Protein; WHAMM, WASP Homolog associated with Actin Membranes and Microtubules.



## INTRODUCTION

The actin cytoskeleton is crucial for controlling intracellular organization and the dynamics of membrane-bound organelles. To coordinate such cellular functions, globular (G-) actin monomers assemble into filamentous (F-) actin polymers (Pollard, 2016). Actin assembly is important in nearly all animal cells and tissues, although distinct physiological systems may rely on different regulatory factors (Vartiainen and Machesky, 2004; Spence and Soderling, 2015; Rivers and Thrasher, 2017). Despite this progress in understanding cytoskeletal activities, direct connections between dysfunctional actin assembly pathways and the pathogenesis of specific diseases are not well characterized.

To ensure that actin assembles when and where it is needed, proteins called nucleators direct the initiation of actin polymerization (Rottner *et al.*, 2017; Gautreau *et al.*, 2022; Lappalainen *et al.*, 2022). In mammals, these nucleators include the Actin-related protein 2/3 (Arp2/3) complex, which cooperates with ~12 activators, termed nucleation-promoting factors (Campellone and Welch, 2010). Most Arp2/3 activators are members of the Wiskott-Aldrich Syndrome Protein (WASP) family (Alekhina *et al.*, 2017; Kabrawala *et al.*, 2020). The WASP, WAVE, and WASH subgroups within this family have been thoroughly studied during plasma membrane dynamics, cell migration, and endocytic trafficking (Kramer *et al.*, 2022). In contrast, the activities of the WHAMM/JMY subgroup have emerged in processes that were overlooked for many years (Campellone *et al.*, 2023). WHAMM (WASP Homolog associated with Actin Membranes and Microtubules) was discovered to promote ER-Golgi transport, endomembrane tubulation, and actin-microtubule interactions (Campellone *et al.*, 2008; Shen *et al.*, 2012; Russo *et al.*, 2016), while JMY was recognized for roles in gene expression, motility, and *trans*-Golgi transport (Shikama *et al.*, 1999; Zuchero *et al.*, 2009; Schluter *et al.*, 2014). More recent studies have revealed that WHAMM and JMY both function in autophagy and apoptosis (Coutts and La Thangue, 2015; Kast *et al.*, 2015; Mathiowetz *et al.*, 2017; Dai *et al.*, 2019; Hu and Mullins, 2019; King *et al.*, 2021; Wu *et al.*, 2021). Although the activities of these two factors in apoptosis appear to lie in cytosolic actin rearrangements (King *et al.*, 2021; King and Campellone, 2023), their participation in autophagy involves organelle remodeling.

Autophagy (formally, macroautophagy) is a mechanism of cytoplasmic digestion wherein double membrane-bound organelles called autophagosomes engulf cytoplasmic material and fuse with lysosomes for degradation (Zhao and Zhang, 2019; Vargas *et al.*, 2023). This process is crucial for organismal development and cellular homeostasis and takes place constitutively, but is also induced by nutrient starvation, proteotoxic stress, and other stimuli (Levine and Kroemer, 2019; Lamark and Johansen, 2021). During autophagosome biogenesis, PI(3)P-rich phagophore membranes surround cytoplasmic cargo (Axe *et al.*, 2008; Devereaux *et al.*, 2013; Mi *et al.*, 2015). This activity involves the ATG8 family of proteins, including the mammalian LC3s (LC3A/B/C) and GABARAPs (GABARAP, GABARAP-L1/L2), which exist as immature forms (e.g., LC3-I) that are cytosolic, and mature phosphatidylethanolamine-conjugated forms (e.g., LC3-II) that are linked to autophagosomal membranes (Mizushima, 2020; Klionsky *et al.*, 2021). Selective autophagy receptors, such as SQSTM1/p62, act as adaptors by binding both LC3 and ubiquitinated cellular "cargo" (Pankiv *et al.*, 2007; Johansen and Lamark, 2020; Vargas *et al.*, 2023). Autophagic flux takes place upon syntaxin-mediated autophagosome fusion with lysosomes and the degradation and recycling of macromolecules (Nakamura and Yoshimori, 2017). Following autolysosomal membrane tubulation, lysosomes can be regenerated, enabling them to maintain cellular proteostasis (Ballabio and Bonifacino, 2020).

A specific function for actin dynamics in autophagy was initially revealed when the interiors of phagophores were found to be shaped by actin assembly in a PI(3)P-dependent manner (Mi *et al.*, 2015). Subsequently, WHAMM and JMY were shown to act at multiple steps in the canonical autophagy pathway. WHAMM binds to PI(3)P, localizes to subdomains of nascent autophagosomes, and is important for efficient LC3 lipidation (Mathiowetz *et al.*, 2017). WHAMM-driven Arp2/3 activation also increases the size of autophagosomes and causes their actin-based rocketing in the cytosol (Kast *et al.*, 2015). JMY binds LC3 and affects autophagosome maturation (Coutts and La Thangue, 2015). Upon activation by LC3, JMY additionally promotes autophagosome rocketing (Hu and Mullins, 2019). WHAMM participates again later in the autophagy pathway by binding $PI(4,5)P_2$ and mediating autolysosome tubulation (Dai *et al.*, 2019; Wu *et al.*, 2021). WHAMM function is ultimately important for the degradation of p62 and turnover of ubiquitinated cargo (Mathiowetz *et al.*, 2017).

Although the founding member of the WASP family was discovered decades ago due to genetic mutations in patients with immunodeficiencies (Derry *et al.*, 1994; Rivers and Thrasher, 2017), surprisingly little is understood about how alterations in other family members contribute to disease. Several mutant versions of WAVE- or WASH-binding proteins have been observed in individuals with neurological or immunological disorders (Kramer *et al.*, 2022; Campellone *et al.*, 2023), but mutations in the WASP-family genes themselves are only beginning to be characterized (Valdmanis *et al.*, 2007; Ropers *et al.*, 2011; Ito *et al.*, 2018; Courtland *et al.*, 2021; Srivastava *et al.*, 2021). *WHAMM* variants play a potential role in disease, as most Amish patients with the rare neurodevelopmental/kidney disorder Galloway-Mowat Syndrome (GMS) harbor a homozygous *WHAMM* mutation that abrogates WHAMM-driven Arp2/3 activation in vitro and leads to autophagy defects in cells (Jinks *et al.*, 2015; Mathiowetz *et al.*, 2017). However, GMS has a complex genetic basis, as Amish patients also possess a homozygous mutation in the nearby *WDR73* gene which is considered to be disease-causing (Jinks *et al.*, 2015). *WDR73* mutations are associated with multiple neurological illnesses (Colin *et al.*, 2014; Ben-Omran *et al.*, 2015; Vodopiutz *et al.*, 2015; Jiang *et al.*, 2017; El Younsi *et al.*, 2019; Tilley *et al.*, 2021), and loss-of-function mutations in many different genes can give rise to GMS or GMS-like conditions (Braun *et al.*, 2017; Rosti *et al.*, 2017; Braun *et al.*, 2018; Arrondel *et al.*, 2019; Mann *et al.*, 2021). Thus, the contribution of WHAMM to health and disease is difficult to discern. In the current study, we generated a null mutation in mouse *Whamm* to better define its role in kidney physiology and cellular autophagy.

## RESULTS

### WHAMM knockout male mice display proximal tubule reabsorption defects

To understand the organismal function of WHAMM, we used a *Whamm* allele with a targeted deletion in exon 3 to generate homozygous WHAMM knockout ($WHAMM^{KO}$) mice (Figure 1A). We then compared the mutant mice to wild type ($WHAMM^{WT}$) littermates in multiple phenotypic analyses. Because Amish GMS patients have kidney abnormalities resulting in proteinuria (Jinks *et al.*, 2015), we first tested the urine from wild type and knockout mice for albuminuria. $WHAMM^{KO}$ males displayed a significant increase in the albumin-to-creatinine ratio (ACR) compared with $WHAMM^{WT}$ males at 24 wk-of-age (Figure 1B). In contrast, ACRs for KO and WT females were statistically indistinguishable from one another (Figure 1B). To determine the kinetics of male albuminuria, we compared the ACRs at 16, 20, and 24-wk timepoints. While $WHAMM^{WT}$ males showed a slight decrease in ACR over time, $WHAMM^{KO}$ males showed a gradual increase in ACR until a statistically significant difference between the WT and KO was reached at 24 wk (Supplemental Figure S1).

To explore whether the inactivation of *Whamm* affected other parameters of kidney function, we next analyzed urinary glucose levels. $WHAMM^{KO}$ male mice displayed significantly higher glucose-to-creatinine ratios (GCR) at 20 and 24 wk (Figure 1C). This phenotype was also sex-specific, as knockout and wild type females were similar to one another (Supplemental Figure S1). The urinary excretion of glucose in males did not appear to be caused by diabetes, as nonfasting plasma glucose levels did not differ between the KO and WT (Figure 1D).

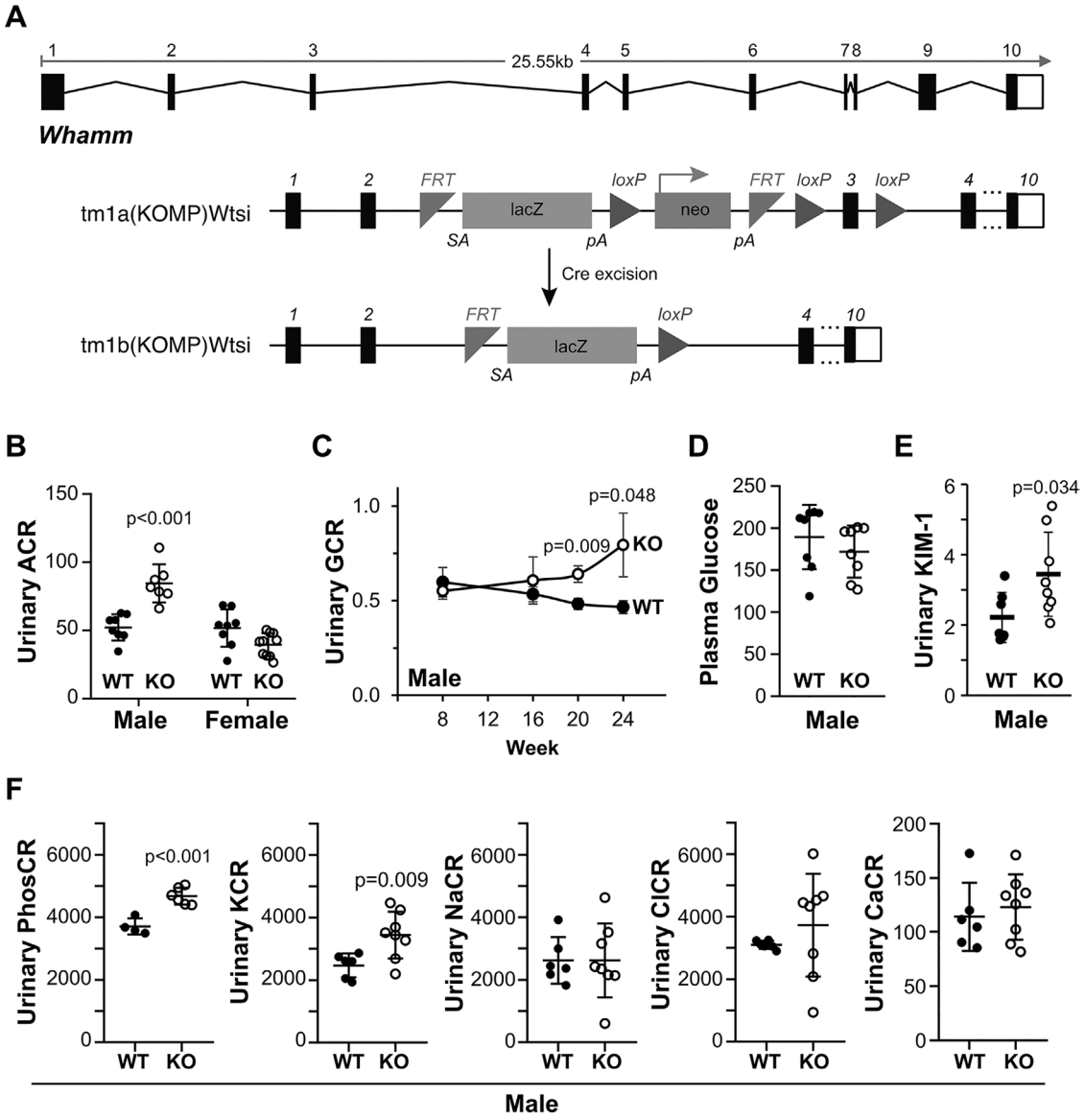


**FIGURE 1:** Male WHAMM$^{KO}$ mice excrete elevated levels of albumin, glucose, KIM-1, phosphate, and potassium in their urine. (A) The mouse *Whamm* gene is 25kb in length and contains 10 exons. A floxed allele containing IRES-*lacZ* and neo cassettes between exons 2 and 3, as well as *loxP* sites between the cassettes and flanking exon 3 was generated. Cre-mediated recombination created a knockout allele. Internal ribosome entry site (IRES); splice acceptor (SA); polyadenylation (pA); flippase recombination target (FRT). (B) Urine samples were collected from male and female wild type (WT; filled circles) or WHAMM knockout (KO; open circles) mice at 24 wk-of-age and subjected to urinalysis. Urinary albumin-to-creatinine (ACR) ratios are plotted. Each circle represents one mouse. Statistical bars display the mean ± SD from $n = 7–10$ mice. (C) Urinary glucose-to-creatinine (GCR) ratios for males from 8 to 24 wk-of-age are plotted. Each point represents the mean ± SE from $n = 6–9$ mice per genotype for each timepoint. (D) Plasma GCR for males at 24 wk-of-age are plotted. Statistical bars display the mean ±SD from $n = 8$ mice. (E) Urinary KIM-1 levels (ng/ml) from male mice at 16 wk are plotted. Each circle represents one mouse. Statistical bars display the mean ± SD from $n = 7–8$ mice. (F) Urinary phosphate (PhosCR), potassium (KCR), sodium (NaCR), chloride (ClCR), and calcium (CaCR) to creatinine ratios are plotted. Each circle represents one male mouse at 24 wk. Statistical bars display the mean ± SD from $n = 4–8$ mice. Significant $p$ values are noted (unpaired $t$ tests).

If the abnormal excretion by knockout mice was due to kidney damage, then other indicators of kidney disease should be present in the urine. We measured the urinary abundance of kidney injury molecule 1 (KIM-1), a biomarker which is upregulated in the proximal tubule and shed from damaged tubular cells (Song *et al*., 2019). KIM-1 levels were significantly elevated in the urine of male WHAMM$^{KO}$ mice compared with their WHAMM$^{WT}$ counterparts (Figure 1E). KIM-1 excretion was generally lower in females than in males, but a subset of WHAMM$^{KO}$ females also showed an increase in urinary KIM-1 (Supplemental Figure 1C). These findings suggest that proximal tubule function is disrupted in mice lacking WHAMM.

Given that multiple molecules were excreted at abnormally high levels when WHAMM was deleted, especially in males, we additionally measured urinary phosphate, potassium, sodium, chloride, and calcium in the 24-wk-old male mice. The WHAMM$^{KO}$ males had a significantly higher urinary phosphate-to-creatinine ratio (PhosCR)

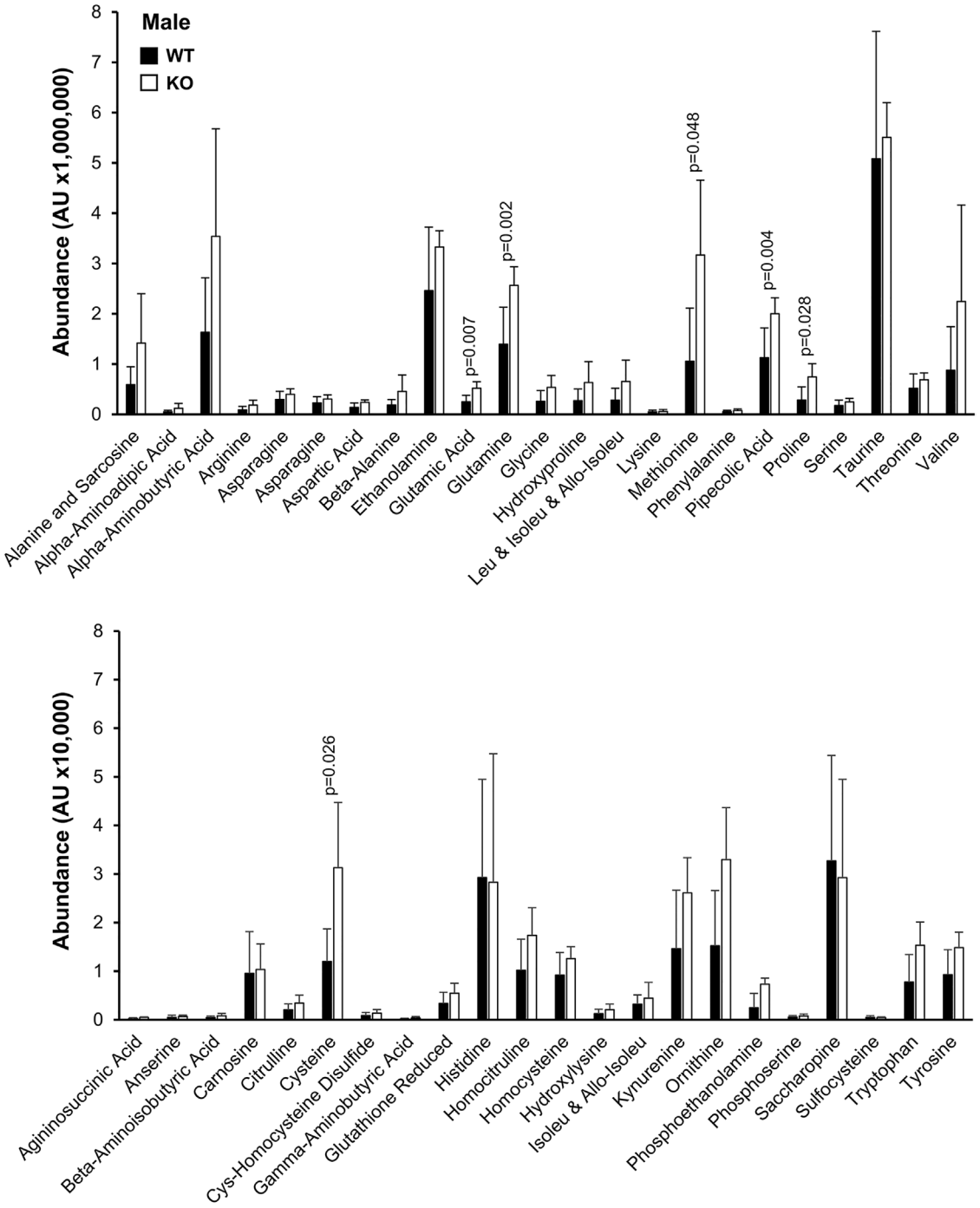


**FIGURE 2:** Male WHAMM$^{KO}$ mice excrete elevated levels of amino acids in their urine. Urine samples were collected from male wild type (WT; black bars) or WHAMM knockout (KO; white bars) mice at 24 wk-of-age, and urinary amino acids were measured using mass spectrometry. AU = arbitrary units. Each bar represents the mean ± SD from $n = 5–6$ mice. Significant $p$ values are noted (ANOVA).

and potassium-to-creatinine ratio (KCR) than the WHAMM$^{WT}$ mice, whereas urinary sodium (NaCR), chloride (ClCR), and calcium (CaCR) did not show differences between the two genotypes of male mice (Figure 1F). Because glucose, phosphate, and potassium are reabsorbed from the filtrate in the proximal tubule, these results are further indicative of a tubular malfunction in the WHAMM$^{KO}$ males.

The WHAMM$^{KO}$ excretion phenotypes are reminiscent of those found in renal Fanconi Syndromes, proximal tubule diseases with diverse genetic bases (Klootwijk *et al.*, 2015; Lemaire, 2021). As amino aciduria is also seen in Fanconi Syndromes, we used mass spectrometry to measure the relative levels of different amino acids in the urine of 24-wk-old knockout and wild type males. The WHAMM$^{KO}$ males showed statistically significant increases in urinary glutamic acid, glutamine, methionine, pipecolic acid, proline, and cysteine (Figure 2). These observations further support the conclusion that WHAMM deficiency causes a Fanconi-like Syndrome in male mice.

### WHAMM deletion alters proximal tubule polarity in male kidneys

Previous work has shown that WHAMM protein is abundant in the human and mouse kidney (Campellone *et al.*, 2008), but the more precise locations of its expression in the nephron have not been described. To assess the cell type-specific mRNA expression pattern of *Whamm*, we surveyed single-cell sequencing data from male and female adult mouse kidneys (Ransick *et al.*, 2019). *Whamm* mRNA was present throughout the proximal tubule of both male and female mice, with its highest expression found in segment two of the proximal tubule of male mice (Supplemental Figure S2). *Whamm* levels in the proximal tubule were higher than those in podocytes but less than those in intercalated type-B cells of the cortical collecting duct (Supplemental Figure S2). Analyses of *Whamm* and other WASP-family and Arp2/3 complex genes indicated that they were all expressed in podocytes and proximal tubules to varying degrees, with the exceptions of *Was* (encoding WASP), *Wasf1* (WAVE1), and *Actr3b* (the Arp3B isoform), which were absent (Supplemental Figure S3). WHAMM expression in the proximal tubule of male mice is, therefore, amenable to a role in tubular reabsorption.

Some proximal tubule disorders have been attributed to endocytic trafficking defects and reductions in quantities of receptor proteins (Norden *et al.*, 2002; Oltrabella *et al.*, 2015; Inoue *et al.*, 2017; Festa *et al.*, 2019; Berquez *et al.*, 2020; Lemaire, 2021). Based on the physiological abnormalities in WHAMM-deficient mice being mostly sex-specific, we focused our efforts on characterizing tissues and cells from males. To assess the amounts of the multiligand endocytic receptor LRP2/Megalin, the tubule-expressed angiotensin-converting enzyme ACE2, the glucose transporter SGLT2, and the phosphate transporter SLC20A1 in WHAMM$^{WT}$ and WHAMM$^{KO}$ males, we isolated their kidneys and generated tissue extracts for immunoblotting. While Megalin levels were highly variable, especially in the knockouts, the relative amount of each receptor protein was generally similar in WHAMM$^{WT}$ and WHAMM$^{KO}$ kidney tissue (Supplemental Figure S4), suggesting that WHAMM deficiency does not dramatically alter the abundance of membrane receptors in the kidney.

For a broad appraisal of kidney structure in the mice, we performed histological analyses of kidney tissue sections after Periodic acid-Schiff (PAS) staining but did not observe any major differences between samples from male WHAMM$^{WT}$ and WHAMM$^{KO}$ animals (Supplemental Figure S5). To more specifically visualize proximal tubule morphology and polarity, we stained kidney sections from WHAMM$^{WT}$ and WHAMM$^{KO}$ males with fluorescent antibodies to Megalin and ACE2 (Figure 3A; Supplemental Figures S6–S9), as both proteins are expected to localize to apical portions of proximal tubule cells (Kerjaschki *et al.*, 1984; Warner *et al.*, 2005). To simultaneously visualize carbohydrates at the apical brush border, we used fluorescently-labeled wheat germ agglutinin (WGA), and to view the microvilli and actin cytoskeleton in tubules we utilized fluorescent antibodies to actin (Kumaran and Hanukoglu, 2020).

In accordance with the immunoblotting results, measurements of Megalin and ACE2 immunofluorescence intensities indicated that wild type and knockout males contained similar amounts of each protein per cluster of tubular cells (Figure 3B; Supplemental Figure S7). However, close inspection of the localization of each protein revealed several differences between the mouse genotypes. Megalin exhibited an apical enrichment in much of the WHAMM$^{WT}$ tissue, but staining was quite variable, and the Megalin-positive tubular clusters in WHAMM$^{KO}$ samples looked more disorganized and displayed a reduced apical concentration or gave a more jagged appearance (Supplemental Figures S6 and S7). ACE2 was consistently apical in WT kidney sections but strikingly nonpolarized in the KO sections (Figure 3A). Quantification of apical and cytoplasmic ACE2 intensity across many tubule clusters in multiple animals demonstrated that ACE2 had an apical-to-cytoplasmic polarity ratio of nearly 3:1 in WHAMM$^{WT}$ samples, whereas the polarity ratio fell to 1:1 in the WHAMM$^{KO}$ (Figure 3B).

The WGA and actin probes also exposed several key differences in the ultrastructure of proximal tubules between the two genotypes of mice. While WHAMM$^{WT}$ samples exhibited a strong WGA staining near the apical regions of proximal tubules, WHAMM$^{KO}$ samples displayed more diffuse WGA staining (Figure 3; Supplemental Figures S6–S9). Moreover, WHAMM$^{WT}$ tissue contained high concentrations of actin in the apical portions of tubules, whereas WHAMM$^{KO}$ tissue had a less polarized and more disorganized actin localization (Figure 3; Supplemental Figures S6–S9). Plotting of the Megalin, ACE2, WGA, and actin fluorescence intensity profiles within tubular clusters showed that the wild type brush borders were demarcated with sharp coincident peaks of WGA and Megalin that were distinct from the broader intervening peaks of ACE2 and actin (Figure 3D; Supplemental Figures S7 and S9). In contrast, knockout tissue was characterized by muted apical intensities of Megalin and WGA, an extreme loss of ACE2 polarization, and erratic actin localization (Figure 3D; Supplemental Figures S7 and S9). Together, our kidney tissue immunoblotting and immunofluorescence data demonstrate that while membrane receptor abundance is relatively normal across WT and KO male mice, receptor polarization and brush border organization in proximal tubule cells is distorted in the absence of WHAMM.

### Lipidation of the autophagosomal protein LC3 is altered in WHAMM$^{KO}$ kidneys

Cellular proteostasis systems are important for maintaining the integrity of proximal tubules (Cybulsky, 2017; Tang *et al.*, 2020), and conditional deletions of Vps34, a key initiator of autophagic membrane biogenesis, alter the urinary proteome and perturb the apical localization of several membrane proteins including ACE2 in mice (Grieco *et al.*, 2018; Rinschen *et al.*, 2022). Because WHAMM plays a role in multiple steps of autophagy (Kast *et al.*, 2015; Mathiowetz *et al.*, 2017; Dai *et al.*, 2019; Wu *et al.*, 2021), we next sought to determine whether some aspect of autophagy might differ in WHAMM$^{KO}$ kidneys. The LC3 and GABARAP classes of proteins are the most widely accepted markers of autophagosomal membranes, and LC3-II and GABARAP-II levels are considered to correlate with autophagosome quantities (Klionsky *et al.*, 2021), so we immunoblotted kidney extracts with polyclonal antibodies that recognize both the immature and mature species of multiple LC3 and GABARAP isoforms.

In male kidneys, immature LC3-I and GABARAP-I levels appeared similar across both WHAMM genotypes (Figure 4A). However, mature lipidated LC3-II was more abundant in WHAMM$^{KO}$ than WHAMM$^{WT}$ kidney tissue (Figure 4A). None of the kidney extracts contained detectable levels of GABARAP-II (Figure 4A). Quantification of the LC3 species revealed that LC3-II was present, on average, in threefold higher amounts in the male knockout than the wild type, and that the LC3 II:I ratio was also substantially greater in the KO males (Figure 4B). In female kidneys, LC3-II levels were not elevated. The only statistically significant difference between KO and WT females was in the LC3 II:I ratio, which was slightly reduced in the WHAMM$^{KO}$ (Supplemental Figure S10). Collectively, these results suggest that the lack of WHAMM leads to altered LC3 modification in the murine kidney, with males experiencing an increase in LC3 lipidation and/or a decrease in LC3-II turnover.

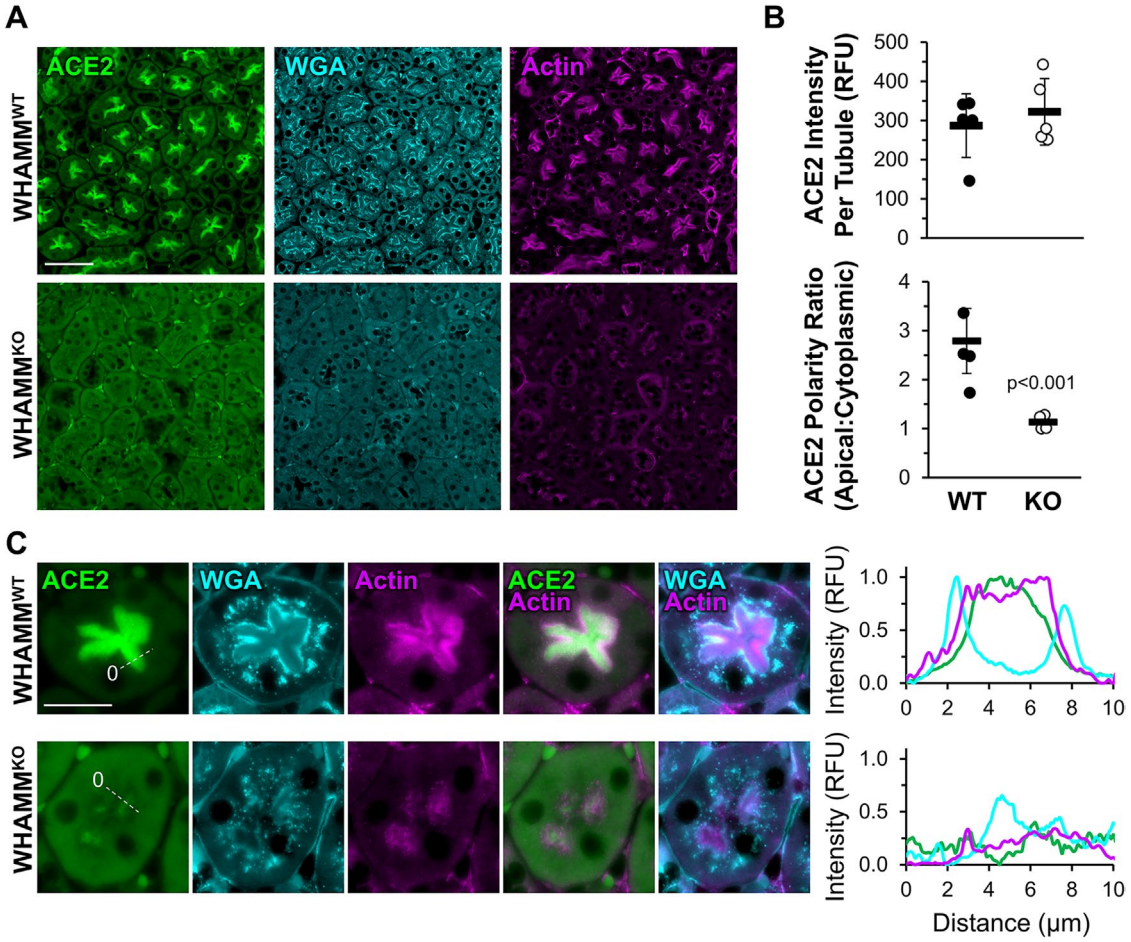


FIGURE 3: Polarized ACE2, WGA, and actin staining in the kidney proximal tubule is reduced in male WHAMM$^{KO}$ mice. (A) Kidney tissue sections from wild type (WHAMM$^{WT}$) or WHAMM knockout (WHAMM$^{KO}$) male mice were stained with ACE2 antibodies (green), WGA (cyan), and actin antibodies (magenta). Scale bar, 50 μm. (B) The ACE2 fluorescence intensity per tubule was calculated in ImageJ. Each circle represents the average ACE2 kidney staining from an individual mouse in which ~ 75 tubules were examined. Statistical bars represent the mean ± SD from $n = 5$ mice. The ACE2 polarity ratio was calculated in ImageJ by dividing the fluorescence intensity in an apical region of the tubule by the intensity in a cytoplasmic region. Each circle represents the average ratio from an individual mouse in which 40 tubules were examined. Statistical bars represent the mean ± SD from $n = 4$ mice. (C) Kidney tissue sections from (A) were used to generate pixel intensity profiles. Lines were drawn through the center of the tubule, and the ACE2, WGA, and actin intensities along the line were plotted. The origin of each line is indicated with a zero. Plotted points represent the normalized mean fluorescence. RFU = relative fluorescence units. Significant $p$ values are noted (unpaired $t$ tests).

### The morphogenesis of autophagic membranes is controlled by WHAMM

To better define the function of WHAMM at the cellular level, we next generated WHAMM-proficient wild type or heterozygous (WHAMM$^{WT}$ or WHAMM$^{HET}$) and WHAMM-deficient (WHAMM$^{KO}$) mouse embryonic fibroblasts (MEFs; Supplemental Figure S11). WHAMM was initially characterized for its ability to activate Arp2/3 complex-dependent actin assembly, bind microtubules, and interact with membranes to promote anterograde transport (Campellone *et al.*, 2008), but F-actin, microtubule, and *cis*-Golgi staining appeared relatively normal in all MEFs under standard culture conditions (Supplemental Figure S11). In contrast, immunoblotting for the autophagy receptor SQSTM1/p62, whose abundance inversely correlates with autophagic flux (Klionsky *et al.*, 2021), demonstrated that male WHAMM$^{KO}$ MEFs harbored significantly more p62 than their WHAMM$^{HET}$ counterparts (Supplemental Figure S11).

Those observations, together with our findings that WHAMM-deficient male mouse kidneys accumulated lipidated LC3, led us to examine how the WHAMM deletion affected autophagy in male MEFs. At steady state, MEFs displayed diffuse LC3 and GABARAP staining without any cytosolic puncta or differences between genotypes (Supplemental Figure S11). This could be the result of low basal levels of autophagy and/or high rates of autophagosome turnover in embryo-derived cells. Therefore, to visualize autophagic structures, we prevented lysosomal degradation by treating MEFs with chloroquine. While WHAMM$^{HET}$ cells formed discrete cup-shaped and ring-like LC3- and GABARAP-positive structures reminiscent of autophagosomes, WHAMM$^{KO}$ cells showed more diffuse and smaller punctate LC3 and GABARAP staining patterns (Figure 5, A and B). Quantification of whole cell mean fluorescence intensities for LC3 and GABARAP demonstrated that the WHAMM deletion increased the intracellular abundance of both ATG8 subfamilies (Figure 5C). In addition, whereas actin localized to LC3- and

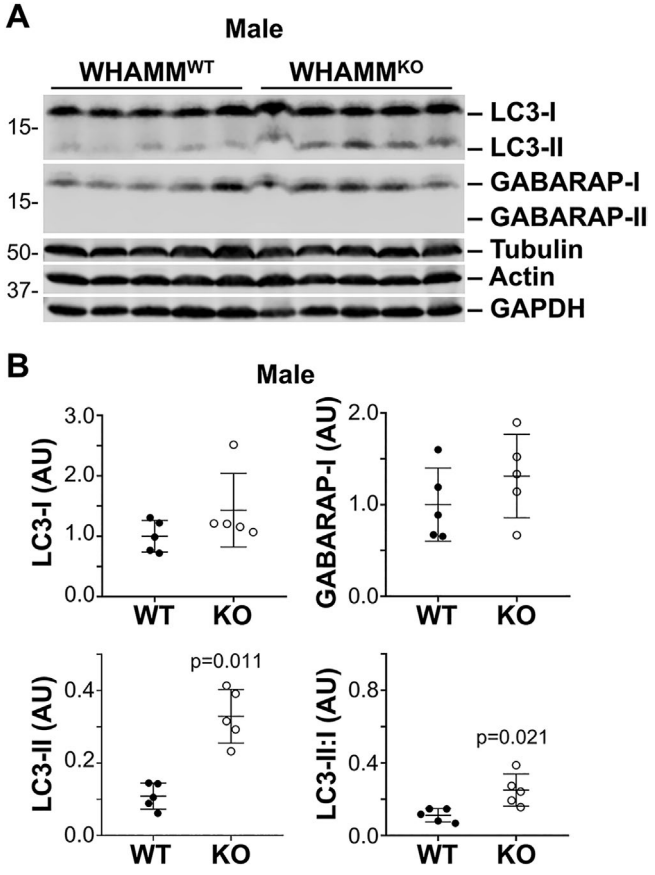


**FIGURE 4:** The lipidated form of the autophagosomal protein LC3 is more abundant in male WHAMM$^{KO}$ kidneys. (A) Kidneys were harvested from five male WHAMM$^{WT}$ and five male WHAMM$^{KO}$ mice. Fifty-microgram extract samples were subjected to SDS–PAGE and immunoblotted with antibodies to LC3, GABARAP, tubulin, actin, and GAPDH. (B) LC3 and GABARAP band intensities in (A) were quantified relative to tubulin, actin, and GAPDH, and the mean normalized values were plotted. The LC3-II:I ratio was calculated by dividing the LC3-II band intensity by the LC3-I band intensity within each nonnormalized sample. Statistical bars represent the mean ± SD from $n = 5$ mice. Significant $p$ values are noted (unpaired $t$ tests).

GABARAP-labeled autophagosomes in WHAMM$^{HET}$ MEFs, little actin was recruited to autophagosomal membranes in WHAMM$^{KO}$ MEFs (Figure 5, A and B). These findings indicate that the permanent loss of WHAMM in MEFs causes defects in both the organization of and actin assembly at LC3- and GABARAP-associated structures.

To determine whether increasing the initiation of autophagy could also influence autophagic membrane morphology differentially in WHAMM-proficient versus WHAMM-deficient cells, we exposed MEFs to the autophagy-inducing mTOR inhibitor rapamycin. While neither WHAMM$^{HET}$ nor WHAMM$^{KO}$ cells displayed any discernible LC3-positive autophagosomes after rapamycin treatment, WHAMM$^{HET}$ cells formed several GABARAP puncta (Figure 5D). Quantification of the number of GABARAP puncta per cell and the puncta-to-cytoplasmic GABARAP intensity ratio revealed that, compared with WHAMM$^{HET}$ MEFs, WHAMM$^{KO}$ MEFs did not effectively shape GABARAP-associated autophagic membranes into discrete puncta (Figure 5D). Overall, the presence of disorganized LC3 and/or GABARAP structures in WHAMM$^{KO}$ MEFs demonstrates the importance of WHAMM in promoting autophagic membrane morphogenesis.

### WHAMM activates the Arp2/3 complex to promote actin assembly, LC3 organization, and autophagy receptor sequestration in proximal tubule cells

While the experiments in MEFs add to the existing literature about WHAMM in autophagy, our in vivo studies point to the kidney proximal tubule as the tissue type in which WHAMM function is most crucial. Therefore, we next studied autophagosome morphogenesis in the HK-2 human proximal tubule cell line. To examine the effects of transient WHAMM depletion, we transfected HK-2 cells with control siRNAs or two independent siRNAs targeting the WHAMM transcript. Immunoblotting of cell extracts verified WHAMM protein knockdowns (Figure 6A). Following treatment of transfected HK-2 cells with chloroquine, control cells displayed LC3-positive circular autophagic structures that were often associated with actin (Figure 6B). In contrast to these cells, but akin to the changes in LC3 morphology and actin assembly observed in WHAMM$^{KO}$ MEFs, WHAMM-depleted HK-2 cells exhibited disorganized LC3 staining and diffuse actin staining (Figure 6B). Fluorescence intensity profiles in control cells showed strong actin recruitment at (Figure 6C, i), around (Figure 6C, ii), and within (Figure 6C, iii; Supplemental Figure S12) LC3-positive vesicles, whereas WHAMM-depleted cells had disorganized LC3 staining with little actin enrichment (Figure 6C). Immunofluorescence using antibodies to the Arp3 subunit confirmed that the Arp2/3 complex also localized at and around LC3-stained structures in control cells and that its localization was diminished in WHAMM-depleted cells (Supplemental Figure S12). Thus, permanent WHAMM deletion in fibroblasts and transient WHAMM depletion in proximal tubule cells both hinder autophagic membrane morphogenesis and actin assembly.

Because the best-characterized molecular activity of WHAMM is to promote Arp2/3 complex-mediated actin polymerization, we next asked whether inhibiting the Arp2/3 complex would impact autophagosome abundance, localization, or morphology in HK-2 cells. We exposed cells to normal media or to media containing the pharmacological Arp2/3 inhibitor CK666, chloroquine, or CK666 plus chloroquine. Fluorescence microscopy revealed that at steady state, both control and CK666-treated cells exhibited diffuse LC3 staining with no noticeable mature autophagic structures (Figure 6D). Upon lysosomal inhibition with chloroquine, LC3-positive rings accumulated throughout the cytoplasm and often associated with actin (Figure 6E). The combination of chloroquine and CK666 also caused LC3-associated structures to accumulate, but in a smaller perinuclear region, with less circular morphologies, and with minimal recruitment of actin (Figure 6E). Quantification indicated that Arp2/3 inhibition significantly reduced the proportion of cells with mature, ring-shaped LC3-positive autophagosomes, the number of LC3 rings per cell, and the amount of actin localizing at or near the autophagic membrane (Figure 6, F and G). Hence, like WHAMM, the Arp2/3 complex is important for the formation of mature, properly shaped autophagosomes.

If the irregular morphologies of LC3-associated membranes are incompatible with efficient autophagosome closure, then the localization of proteins involved in autophagosome-lysosome fusion should be altered. Syntaxin-17 (STX17) is a SNARE protein recruited to autophagosomes upon closure and is important for their subsequent fusion with lysosomes (Itakura *et al.*, 2012; Tsuboyama *et al.*, 2016; Koyama-Honda and Mizushima, 2022). To examine the effects of WHAMM depletion on autophagosome closure, we transfected HK-2 cells with siRNAs, inhibited lysosomes with chloroquine, and stained the cells with antibodies to LC3 and STX17 (Figure 7A). Approximately 75% of siControl cells possessed at least one STX17-positive vesicle, and on average each cell had two to three such

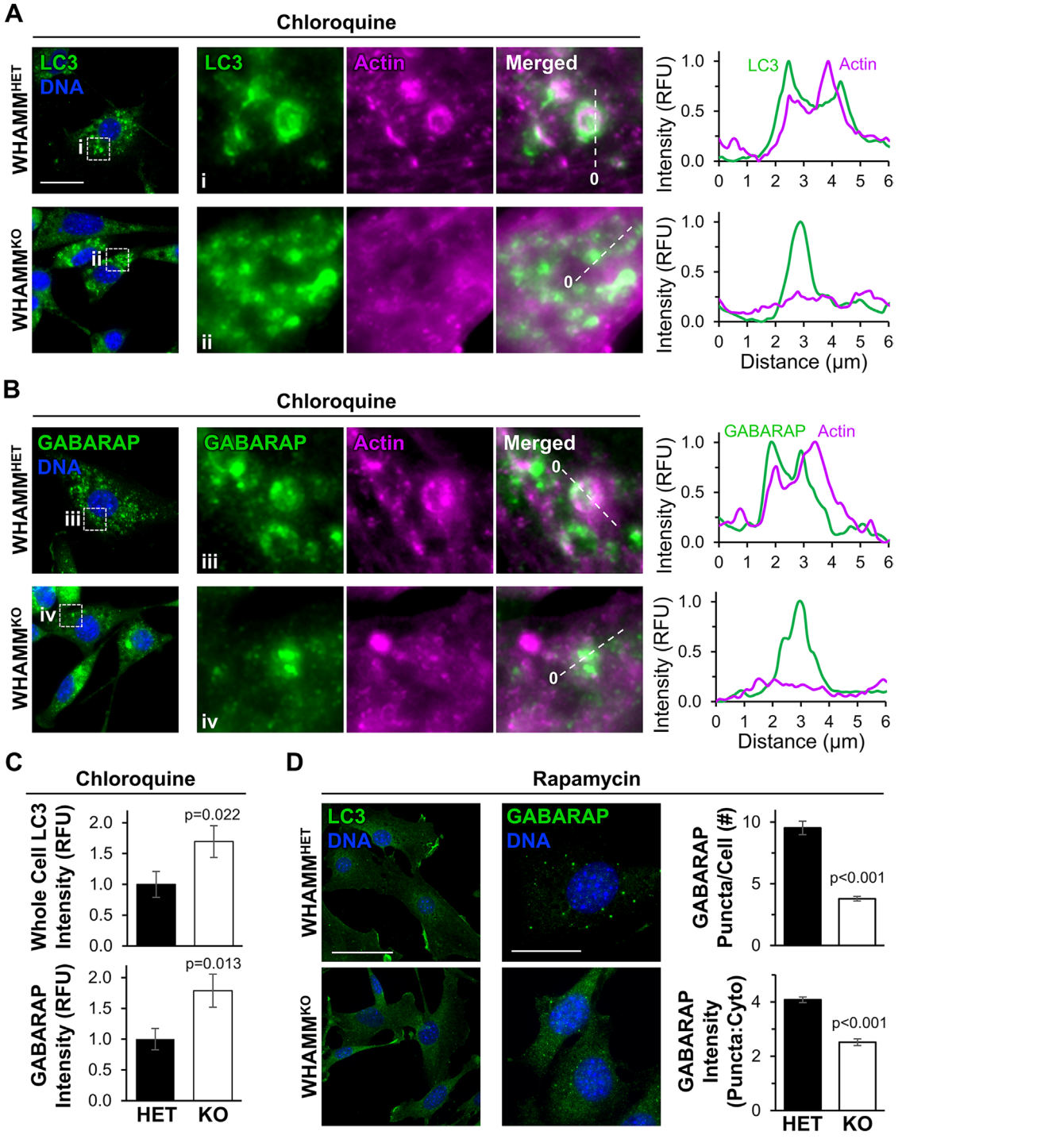


FIGURE 5: Autophagosome organization and actin recruitment are altered in WHAMM-deficient fibroblasts. (A and B) Male heterozygous (WHAMM$^{HET}$) and WHAMM knockout (WHAMM$^{KO}$) MEFs were treated with chloroquine for 16 h before being fixed and stained with LC3 antibodies (green), an actin antibody (magenta), and DAPI (DNA; blue). Scale bar, 25 μm. Magnifications highlight areas of (i, iii) actin recruitment to LC3- or GABARAP-positive structures in WHAMM$^{HET}$ cells and (ii, iv) a lack of actin enrichment at autophagosomal puncta in WHAMM$^{KO}$ cells. Lines were drawn through the images to measure pixel intensity profiles. The origin of each line is indicated with a zero. (C) Mean LC3 and GABARAP fluorescence values per cell were measured in ImageJ. Each bar represents the mean ± SD from $n = 3$ experiments (145–161 cells per bar). (D) WHAMM$^{HET}$ and WHAMM$^{KO}$ MEFs were treated with rapamycin for 16 h before being fixed and stained with LC3 or GABARAP antibodies (green) and DAPI (DNA; blue). Scale bars, 50 μm, 25 μm. The number (#) of GABARAP puncta per cell was counted manually. Each bar represents the mean ± SD from $n = 3$ experiments (30 cells per genotype per experiment). To calculate the puncta:cytoplasmic ratio of GABARAP fluorescence intensities, the mean fluorescence of GABARAP puncta was divided by the mean cytoplasmic GABARAP fluorescence in ImageJ. Each bar represents the mean ± SD from $n = 3$ experiments (four to seven puncta per cell; six to eight cells per genotype per experiment). Significant $p$ values are noted (unpaired $t$ tests).

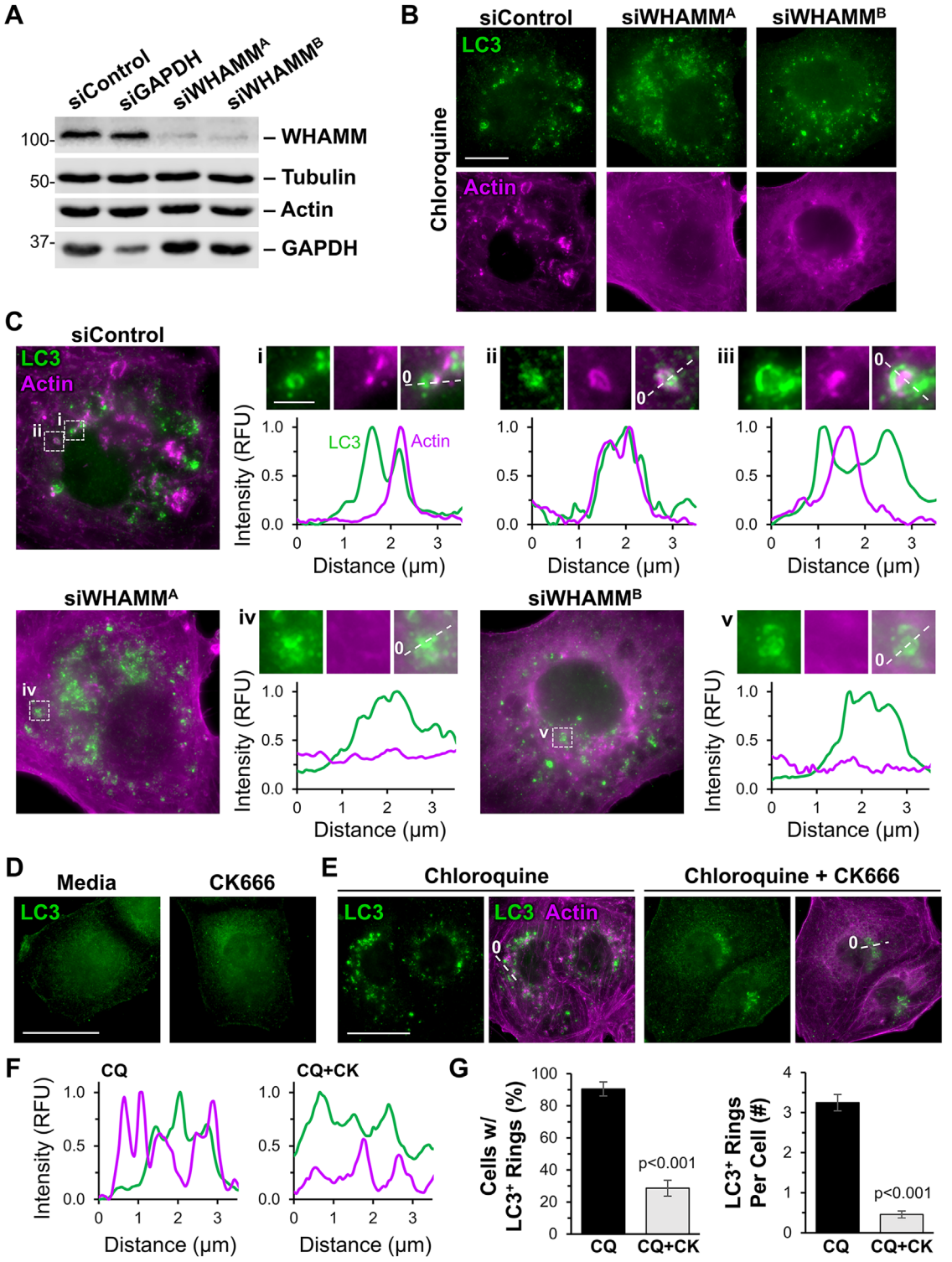


FIGURE 6: WHAMM depletion or Arp2/3 complex inhibition disrupts LC3 and actin organization in proximal tubule cells. (A) Human kidney proximal tubule (HK-2) cells were transfected with control siRNAs, GAPDH siRNAs, or independent siRNAs targeting the WHAMM transcript before immunoblotting with antibodies to WHAMM, tubulin, actin, and GAPDH. (B) Transfected HK-2 cells were exposed to media containing chloroquine for 6 h before being fixed and stained with antibodies to LC3 (green) and actin (magenta). Scale bar, 10 μm. (C) Lines were drawn through the magnified images from (B) to measure pixel intensity profiles. Magnifications highlight areas of (i–iii) actin recruitment to LC3-positive structures in siControl cells and (iv–v) a lack of actin enrichment at autophagosomal puncta in siWHAMM cells. The parent image for (iii) is shown in Supplemental Figure S12. Scale bar, 2 μm. (D) HK-2 cells were treated with normal media or media containing CK666 for 6 h before being fixed and stained with LC3 antibodies. (E) Cells were treated with chloroquine, or chloroquine plus CK666 for 6 h before being fixed and stained with antibodies to LC3 (green) and actin (magenta). (F) Lines were drawn through the images in (E) to measure pixel intensity profiles. (G) The percentage (%) of cells with LC3-positive rings and the # of LC3-positive rings per cell were quantified. Each bar represents the mean ± SD from $n = 3$ experiments (150 cells per bar). Significant $p$ values are noted (unpaired $t$ tests).

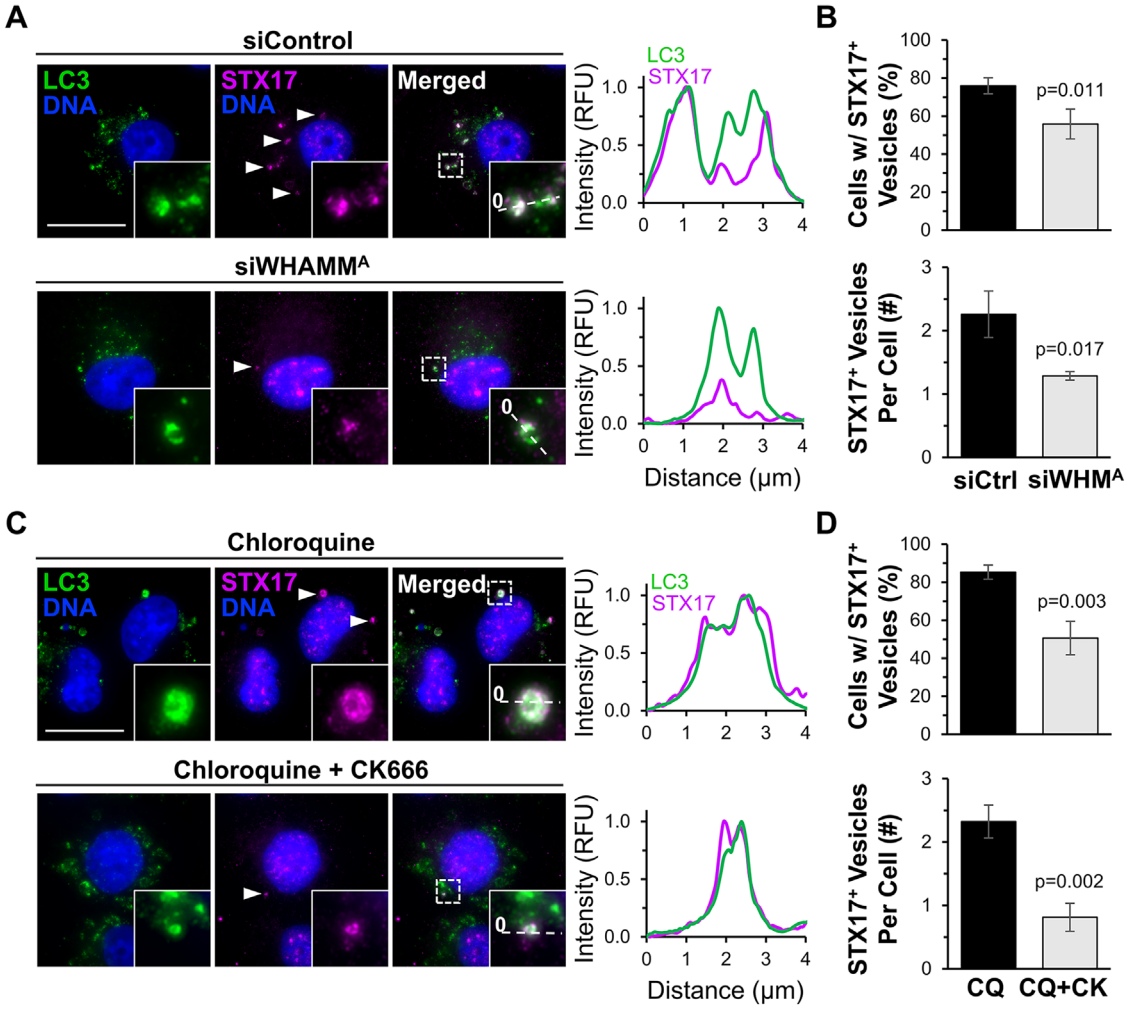


FIGURE 7: WHAMM and the Arp2/3 complex are crucial for autophagosome closure. (A) HK-2 cells transfected with control siRNAs or siRNAs targeting WHAMM were treated with chloroquine for 6 h before being fixed and stained with STX17 antibodies (magenta), an LC3B antibody (green), and DAPI (DNA; blue). Arrowheads highlight STX17-positive vesicles. Lines were drawn through the magnified images to measure pixel intensity profiles. (B) The percentage of cells with STX17-positive vesicles and the # of STX17-positive vesicles per cell were quantified. Each bar represents the mean ± SD from $n = 3$ experiments (104–108 cells per bar). (C) HK-2 cells were treated with chloroquine, or chloroquine plus CK666 for 6 h before being fixed, stained, and analyzed as above. (D) The percentage of cells with STX17-positive vesicles and the # of STX17-positive vesicles per cell were quantified. Each bar represents the mean ± SD from $n = 3$ experiments (230 cells per bar). Significant $p$ values are noted (unpaired $t$ tests). Scale bars, 20 μm.

vesicles (Figure 7B). Conversely, the siWHAMM treatment reduced both the percentage of cells containing STX17-positive vesicles and the number of STX17-associated vesicles per cell (Figure 7B).

To further evaluate STX17 localization in the presence and absence of Arp2/3 complex activity, we treated HK-2 cells with chloroquine in conjunction with either DMSO or CK666 and again stained the cells for STX17 and LC3 (Figure 7C). As with WHAMM depletion, Arp2/3 inhibition reduced both the fraction of cells containing STX17-positive vesicles and the amount of STX17-positive vesicles per cell, while the vesicles that were present appeared smaller (Figure 7D). These findings support the conclusion that efficient autophagosome closure is reliant on WHAMM and the Arp2/3 complex.

In the canonical selective autophagy pathway, LC3-decorated membranes interact with autophagy receptors, which are bound to ubiquitinated cargo (Vargas *et al.*, 2023). So we next asked whether the steps of receptor-ubiquitin or receptor-LC3 interactions were influenced by the Arp2/3 complex. SQSTM1/p62, an autophagy receptor with a wide range of selective targets, has been shown to associate with ubiquitinated protein aggregates that are destined for autophagic degradation (Pankiv *et al.*, 2007; Sarraf *et al.*, 2020). We, therefore, induced the production of truncated proteins in HK-2 cells using puromycin and assessed the effects of Arp2/3 inhibition on the recruitment of p62 to ubiquitinated material. Puromycin caused the formation of bright foci of ubiquitinated proteins, and p62 localized to the ubiquitin foci in the absence or presence of CK666 (Supplemental Figure S13), indicating that Arp2/3 inactivation does not prevent the association between ubiquitinated cargo and p62.

To examine the step of receptor-LC3 engagement, we evaluated the recruitment of p62 to LC3. As expected, when cells were treated with chloroquine, p62 localized to both punctate and ring-like LC3-positive autophagic structures (Figure 8, A and B). However, when cells were treated with chloroquine in combination with WHAMM siRNAs, LC3 and p62 colocalized at much smaller punctate structures, and additional LC3-independent p62 puncta became apparent (Figure 8A). Further, when cells were subjected to concurrent

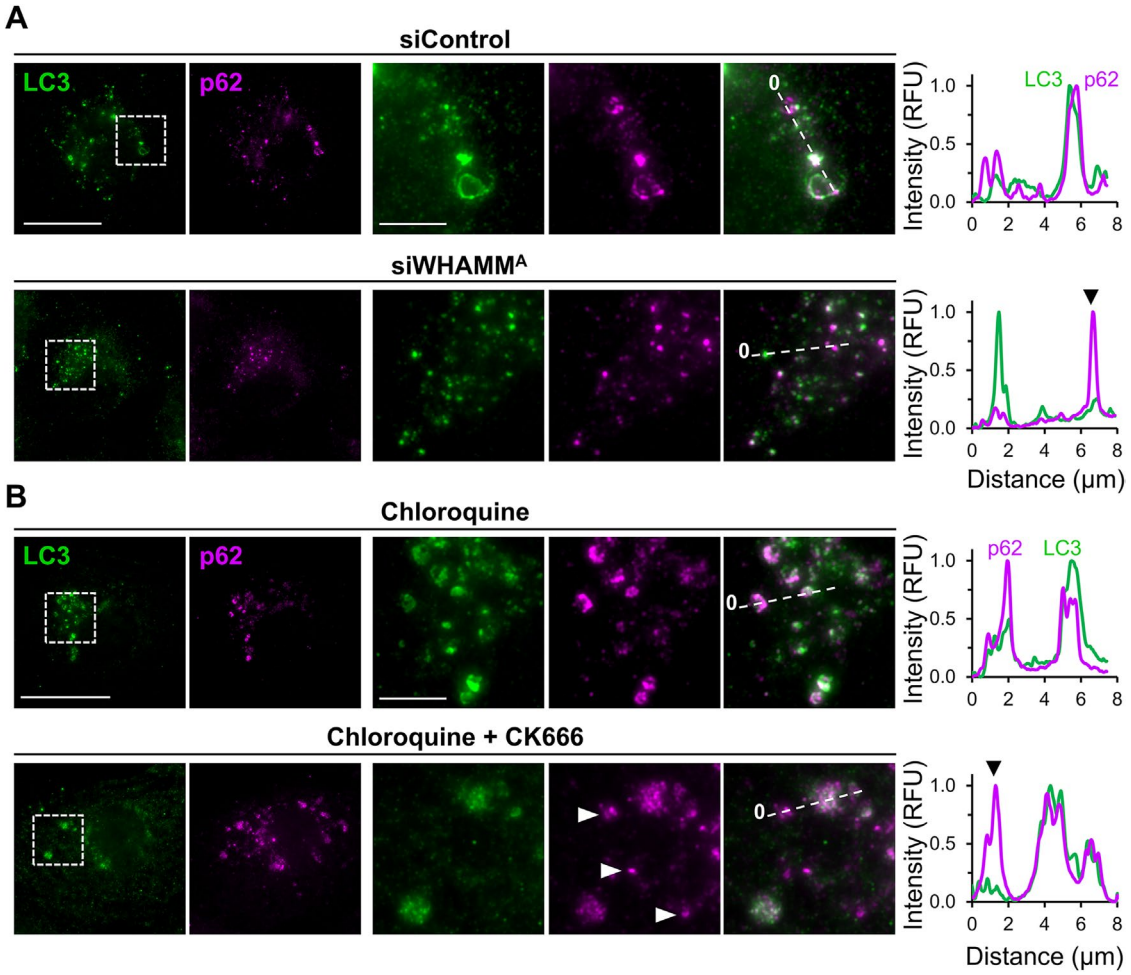


FIGURE 8: WHAMM and the Arp2/3 complex are important for cargo receptor recruitment to LC3-associated membranes. (A) HK-2 cells transfected with control siRNAs or siRNAs targeting WHAMM were treated with chloroquine for 6 h before being fixed and stained with antibodies to LC3 (green) and p62 (magenta). Arrowheads highlight LC3-independent p62 structures. Lines were drawn through the magnified images to measure pixel intensity profiles. (B) HK-2 cells were treated with media containing chloroquine or chloroquine plus CK666 for 6 h before being fixed, stained, and analyzed as above. Lines were drawn through the magnified images to measure pixel intensity profiles. Scale bars, 20 μm, 5 μm.

chloroquine and CK666 treatment, LC3 and p62 could be found together in disorganized structures, and extra p62 puncta were again present (Figure 8B). These results suggest that autophagosomal membrane remodeling is coupled to receptor capture and that this process is inefficient without WHAMM and an active Arp2/3 complex.

To connect the observations that both WHAMM and the Arp2/3 complex impact actin assembly at autophagic membranes, we studied actin organization in HK-2 cells expressing a LAP (localization and affinity purification) tagged version of either wild type WHAMM or a mutant WHAMM lacking a critical Arp2/3-binding residue (WHAMM W807A; Campellone *et al.*, 2008). As predicted, wild type WHAMM localized to LC3-positive structures, and actin was enriched around these autophagic membranes (Figure 9A). Similar to cells depleted of WHAMM (Figure 6), cells expressing the WHAMM W807A mutant protein displayed more diffuse cytoplasmic LC3 staining (Figure 9A). In cases where small LC3 puncta were observed, the puncta associated with WHAMM W807A but lacked actin (Figure 9A). Together, these results show that WHAMM stimulates Arp2/3 complex-mediated actin assembly to control autophagic membrane morphogenesis and cargo receptor sequestration.

## DISCUSSION

Actin nucleation factors are important players in a variety of processes that are crucial for cellular function. However, their roles in organismal health and disease have been relatively understudied. Deletion of several WASP-family members, including N-WASP, WAVE2, and WASH, results in embryonic lethality in mice (Snapper *et al.*, 2001; Yan *et al.*, 2003; Gomez *et al.*, 2012; Xia *et al.*, 2013), demonstrating the essentiality of these factors in mammalian development. Similar animal studies of WASP-family proteins from the WHAMM/JMY subgroup had not been previously explored, so we focused our investigation on the impact of WHAMM inactivation in mice. Here we establish the importance of WHAMM in kidney physiology in vivo and in autophagosome closure during cargo capture in proximal tubule cells.

The inherited neurodevelopmental and kidney disorder GMS is associated with several different *WDR73* mutations (Colin *et al.*, 2014; Ben-Omran *et al.*, 2015; Vodopiutz *et al.*, 2015; Jiang *et al.*, 2017; El Younsi *et al.*, 2019; Tilley *et al.*, 2021), but in patients from Amish communities, 26 of 27 affected individuals were found to be doubly homozygous for loss-of-function mutations in both *WDR73* and *WHAMM*, with one *WHAMM* heterozygous individual presenting

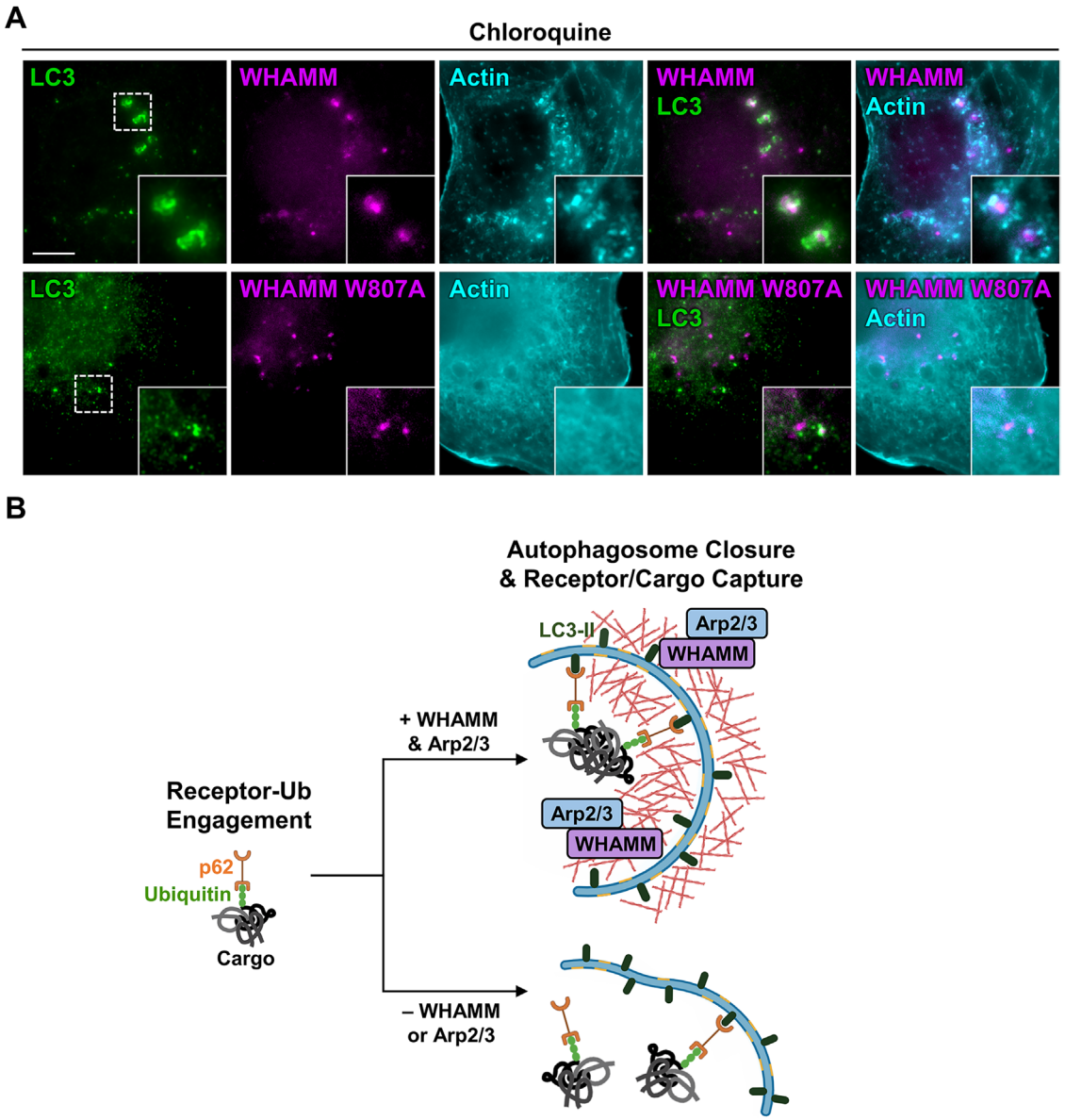


FIGURE 9: WHAMM promotes Arp2/3 complex-mediated actin assembly during autophagosomal membrane morphogenesis. (A) HK-2 cells expressing LAP-WHAMM wild type or a LAP-WHAMM W807A mutant deficient in Arp2/3 activation (both in magenta) were fixed and stained with antibodies to LC3 (green) and actin (cyan). Scale bar, 10 μm. (B) Model for WHAMM and Arp2/3 complex function in autophagosome closure during cargo/receptor capture. Aggregated protein cargo (gray) is ubiquitinated (green) before its engagement by autophagy receptors like p62 (orange). WHAMM (purple) and the Arp2/3 complex (blue) promote the assembly of actin filaments (red) necessary for autophagosome membrane morphogenesis. In the absence of WHAMM or the Arp2/3 complex, actin assembly at autophagic membranes is abrogated, resulting in inefficient receptor recruitment to LC3 and incomplete autophagosome closure.

with neurological symptoms but lacking renal symptoms (Jinks *et al.*, 2015; Mathiowetz *et al.*, 2017). Given the genotypic and phenotypic variability of GMS, the extent to which WHAMM inactivation might modify the clinical outcomes in Amish patients has been unclear. Our current study begins to untangle the complexities of Amish GMS by showing that a targeted mutation in *Whamm* by itself can cause kidney dysfunction in mice.

An elevated urinary protein:creatinine ratio and end-stage renal disease affect the majority of Amish GMS patients (Jinks *et al.*, 2015). Recently, a targeted deletion in mouse *Wdr73* was found to be embryonic lethal (Li *et al.*, 2022). However, a conditional *Wdr73* deletion in podocytes, terminally differentiated cells required for filtration in the glomerulus, yielded live mice. Such animals did not have any detectable kidney phenotypes until chemically induced glomerular injury caused albuminuria (Li *et al.*, 2022). These results contrast the deletion of *Whamm* in mice, which is not lethal, but results in male-specific excretion of a low molecular weight protein, multiple solutes, and amino acids in the urine. Thus, while the molecular and cellular basis of GMS pathogenesis still requires much investigation, our characterization of kidney abnormalities in WHAMM-deficient mice supports the idea that the Amish *WHAMM* mutation may be a modifier in the nephrotic aspects of GMS.

Earlier studies in mice indicated that the WASP-family member N-WASP is also important for kidney function (Schell *et al.*, 2013;

Schell *et al.*, 2018). N-WASP regulates Arp2/3- and actin-driven membrane protrusions in podocytes, and deletion of Arp3 increases urinary excretion of albumin (Schell *et al.*, 2018). Our current studies with WHAMM knockout mice provide new evidence that the WASP family also contributes to kidney physiology in a different anatomical location, the proximal tubule, which is crucial for reabsorption of small molecules from the filtrate.

The excretion profiles observed in WHAMM-deficient mice are reminiscent of those in other proximal tubule disorders, collectively referred to as Fanconi Syndromes (van der Wijst *et al.*, 2019; Lemaire, 2021). Dent disease type II (Hoopes *et al.*, 2005; Utsch *et al.*, 2006) and Lowe Syndrome (Zhang *et al.*, 1995; Bockenhauer *et al.*, 2008; Mehta *et al.*, 2014) are X-linked Fanconi disorders caused by mutations in the *OCRL* gene. *OCRL* encodes a lipid phosphatase, and loss of its enzymatic activity results in the accumulation of PI(4,5)$P_2$, which leads to defects in endosomal trafficking and autophagy (Vicinanza *et al.*, 2011; De Leo *et al.*, 2016; Daste *et al.*, 2017; De Matteis *et al.*, 2017). Given the endocytic and receptor degradation anomalies identified in Lowe Syndrome cells, we tested whether the levels of reabsorption receptors were altered in WHAMM$^{KO}$ kidneys but found no gross changes in receptor abundance. However, the irregular distribution of Megalin, decrease in apical ACE2, and distorted brush border staining with WGA and actin are suggestive of defects in proximal tubule organization, polarity, or membrane trafficking in WHAMM$^{KO}$ tubules. Interestingly, alterations in the urinary proteome, proximal tubule reabsorption, and ACE2 localization have also been observed upon disruption of Vps34, a PI-3 kinase with critical roles in autophagosome biogenesis and endocytic trafficking (Grieco *et al.*, 2018; Rinschen *et al.*, 2022).

WHAMM was first studied for its functions in microtubule binding, anterograde transport, and Golgi morphogenesis (Campellone *et al.*, 2008), but stainings of WHAMM$^{KO}$ MEFs indicated that microtubule and Golgi organization were relatively normal. Taken together with the observations that Amish GMS patient cells have more dramatic defects in autophagosomes than secretory organelles (Mathiowetz *et al.*, 2017), we focused our attention on autophagy. Previous localization and loss-of-function approaches in human epithelial cells, fibroblasts, monkey kidney cells, and GMS patient samples demonstrated the importance of WHAMM early in autophagy during the steps of autophagosome biogenesis, enlargement, and movement (Kast *et al.*, 2015; Mathiowetz *et al.*, 2017). Additional work in human and rat kidney cell lines showed that WHAMM also plays a role later in autophagy by promoting autolysosome tubulation and turnover (Dai *et al.*, 2019; Wu *et al.*, 2021).

Our current study evaluated several autophagy-related parameters in mouse kidneys, mouse fibroblasts, and human proximal tubule cells to link the physiological dysfunction in vivo with alterations in autophagy in vitro. Higher levels of lipidated LC3 in male WHAMM$^{KO}$ kidney tissue first suggested that changes in autophagy accompanied the deficiencies in reabsorption. Fibroblasts generated from WHAMM-proficient or knockout mouse embryos next demonstrated that permanent WHAMM deletion not only resulted in higher overall cellular levels of the LC3 and GABARAP classes of ATG8-family proteins, but also caused aberrations in autophagosomal membrane morphology and a reduction in actin recruitment. In proximal tubule cells, WHAMM and its actin nucleating binding partner, the Arp2/3 complex, were also crucial for the proper morphogenesis and closure of LC3-associated autophagosomes. These results give rise to a model in which WHAMM activates Arp2/3-mediated actin assembly to shape autophagosomal membranes in such a way that allows them to effectively capture autophagy receptors like p62 (Figure 9B). Without WHAMM or the Arp2/3 complex, receptor sequestration becomes inefficient, and the misshapen and incompletely sealed LC3-associated membranes accumulate because their subsequent fusion with lysosomes is impaired.

The numerous functions of WHAMM throughout the autophagy pathway are likely coordinated based on the expression profiles of other proteins that regulate the initiation and progression of multiple degradation pathways. Genetically programmed, epigenetically modulated, or even stochastic changes in such regulatory factors probably determine when and where WHAMM function is most important in a particular cell type. Moreover, different compensatory changes that occur when WHAMM is permanently deleted versus transiently depleted add an additional layer of complexity to deciphering its usual cellular responsibilities. The complicated nature of mammalian protein homeostasis systems and their many potential connections to the actin assembly machinery are underscored by diversity in the repertoires of the (6) LC3/GABARAP isoforms and the (5) basic autophagy receptors (Lazarou *et al.*, 2015; Nguyen *et al.*, 2016), and perhaps even in the WASP-family members (e.g., WHAMM and JMY) themselves. In the case of mice housed in standard laboratory conditions, the crucial functions for WHAMM appeared anatomically in the kidney proximal tubule and molecularly in LC3/GABARAP-associated autophagosome morphogenesis and closure.

The distinct excretion phenotypes in male versus female WHAMM$^{KO}$ mice, and the fact that tissue from only male knockouts showed substantial increases in LC3 lipidation, highlight a sex-specific relationship between kidney physiology and molecular malfunctions in autophagy. The reasons for this male specificity are unclear, but other sex-dependent discrepancies in vivo have been attributed to differences in the distribution and/or abundance of transporters throughout the nephron (Veiras *et al.*, 2017; Harris *et al.*, 2018; Li *et al.*, 2018; Hu *et al.*, 2020; Torres-Pinzon *et al.*, 2021). Anatomically, males have a greater density of proximal tubules in the cortex, whereas in females the collecting duct comprises a larger volume (Harris *et al.*, 2018). Modeling further suggests that a smaller transport area and varied expression of transporters results in less tubular reabsorption in females (Li *et al.*, 2018). Autophagy rates also differ between males and females (Shang *et al.*, 2021). It is worth noting, however, that the presence of elevated urinary KIM-1 levels in both male and female WHAMM$^{KO}$ mice raises the possibility that WHAMM inactivation may have some influence on kidney health irrespective of sex. Perhaps female kidney disease will become more apparent as the mice age or if they are exposed to experimental stressors. Future work on the mechanisms regulating autophagy in the proximal tubule and other portions of the kidney will likely be required to better understand the sex-based differences in kidney physiology arising from the loss of WHAMM.

Lowe Syndrome is X-linked, and excessive actin polymerization on multiple organelles is a prominent feature in cells from patients with this disorder (Suchy and Nussbaum, 2002; Vicinanza *et al.*, 2011; Festa *et al.*, 2019; Berquez *et al.*, 2020). Alterations in PI(3)P and PI(4,5)$P_2$ membrane composition are key drivers of signaling to the actin nucleation machinery in this context, and N-WASP is at least partly responsible for the ectopic actin assembly (Vicinanza *et al.*, 2011; Daste *et al.*, 2017). However, WHAMM is also capable of binding to PI(3)P (Mathiowetz *et al.*, 2017) and PI(4,5)$P_2$ (Dai *et al.*, 2019). So, on one hand it is tempting to speculate that WHAMM-mediated Arp2/3 activation may influence the excess cytoskeletal rearrangements and trafficking modifications that take place in Lowe Syndrome cells, while on the other hand, reduced actin

assembly may underlie the autophagy defects in WHAMM-depleted cells. This combination of previous data and our new findings are consistent with the idea that either over- or underactive actin assembly pathways can cause similar tubular reabsorption problems. Thus, proximal tubule function is governed by exquisitely tight spatiotemporal control of phospholipid signaling to the actin polymerization machinery. Future studies that connect key autophagy regulators with actin nucleation factors, therefore, hold promise for determining how proteostasis pathways and cytoskeletal activities collaborate in healthy kidneys and how their functions are altered during distinct diseases.

## MATERIALS AND METHODS

Request a protocol through *Bio-protocol*.

### Ethics statement

All animal experiments were performed in accordance with the National Institutes of Health Guide for the Care and Use of Laboratory Animals and were approved by The Jackson Laboratory's Animal Care and Use Committee. Research with biological materials was approved by the UConn Institutional Biosafety Committee. This study did not include research with human subjects.

### Mice

A floxed *Whamm* allele generated by the Knockout Mouse Project (genome.gov/17515708) incorporated SA-IRES-*lacZ*-pA and *neo* cassettes between *Whamm* exons 2 and 3, with *loxP* sites located between the two cassettes and following exon 3. Cre-mediated recombination using the B6.C-Tg(CMV-Cre)1Cgn/J strain resulted in the excision of *neo* and exon 3, giving rise to a *Whamm* knockout allele. These B6N(Cg)-*Whamm*$^{tm1b(KOMP)Wtsi}$/3J mice were obtained from The Jackson Laboratory (JAX stock JR#027472). Animals were maintained on pine shavings and given a standard rodent diet (LabDiet 5KOG) and acidified water in a pathogen-free room that was maintained at 21°C with a 12 h light/dark cycle (6 am to 6 pm). Experimental animals were generated by mating heterozygous knockout (WHAMM$^{HET}$) mice and selecting homozygous knockout (WHAMM$^{KO}$) offspring and their wild type (WHAMM$^{WT}$) littermates. Genotyping primers were designed to amplify a 221 bp fragment of the wild type *Whamm* allele or a 222 bp fragment of the knockout *Whamm* allele (Supplemental Table S1). All mice were sacrificed during the SARS-CoV-2 pandemic in 2020. Sperm is cryopreserved at JAX.

### Mouse Phenotyping

Spot urine and blood were collected at 8, 16, 20, and 24 wk-of-age. Urinary albumin, glucose, phosphate, potassium, sodium, chloride, calcium, and creatinine, and plasma glucose were measured using a Beckman Coulter DxC 700 AU chemistry analyzer. For relative quantification of amino acids in the urine, a LC–MS/MS Selected Reaction Monitoring (SRM) method was performed using a Thermo Fisher Scientific TSQ Endura equipped with a Vanquish UPLC based on Thermo Fisher's technical note 65382 adapted for smaller volumes of urine. Briefly, SRM transitions were detailed in the TraceFinder software and then verified with the Metabolomics Amino Acid Mix Standard (Cambridge Isotope Laboratories) for unique transitions. 10 µL of urine was precipitated with 30% sulfosalicylic acid (final concentration 10%) and vortexed for 30 s. Samples were allowed to precipitate for 30min at 4°C and centrifuged to pellet protein. Supernatant was then mixed with internal standard and diluent mixture. 4 µL of this final solution was injected into the platform. Chromatographic separation was performed over 18 min, with an Acclaim Trinity mixed mode column. Buffer A was ammonium formate in water, pH ~3. Buffer B was acetonitrile with ammonium formate, pH ~3. Separation was achieved with a two-part separation and flow rate increase. Detection of each of the 52 transitions was performed with the TSQ Endura triple quadruple mass spectrometer. Data was acquired in SRM mode using a resolution of 0.7 m/z full width at half maximum with a 500 ms cycle time. Data were processed using Tracefinder 4.1 software. KIM-1 was measured in the urine from mice at 16 wk-of-age using a Mouse KIM-1 Quantikine ELISA Kit (MKM100, R&D Systems). Urine samples from other timepoints were not available because they were depleted during the previous chemical analyses.

### Bioinformatics

Gene expression maps from adult mice were created using Kidney Cell Explorer (Ransick *et al.*, 2019). This searchable database (cello.shinyapps.io/kidneycellexplorer/), consisting of single cell RNA-sequencing data clustered into distinct anatomical regions ("metacells") of the nephron, was used to generate heat maps of the normalized average expression of genes (average expression) as well as the proportion of cells expressing a gene (expressed proportion) within each metacell.

### Kidney Histology and Immunostaining

For histological analyses, kidneys were collected from 25-wk-old WHAMM$^{WT}$ and WHAMM$^{KO}$ mice in 10% neutral buffered formalin, embedded in paraffin, and subjected to PAS staining. Slides can be viewed at https://images.jax.org/webclient/?show=dataset-2763. For immunostaining, 5 µm kidney sections were mounted onto charged glass slides, deparaffinized in Histo-Clear (National Diagnostics) twice, 100% ethanol twice, 95% ethanol twice, and 70% ethanol, then rehydrated in deionized water. Antigen retrieval was performed at 95°C in citrate buffer (20 mM citric acid, 93 mM sodium citrate in water) pH 6.0 for 30 min, and slides were cooled to room temperature before three phosphate-buffered saline (PBS) washes. Tissue samples were incubated in blocking buffer (PBS containing 1% bovine serum albumin [BSA], 10% goat serum, 0.1% Tween-20) for 2 h at room temperature, washed once with PBS, probed with primary antibodies (Supplemental Table S2) for 10 h at 4°C, washed three times, and treated with AlexaFluor-conjugated secondary antibodies, tetramethylrhodamine-labeled WGA, and DAPI (Supplemental Table S2) for 2 h at 4°C, followed by three PBS washes and mounting using ProLong Gold (Invitrogen) and 18-mm square glass coverslips. Slides were imaged as described below. WHAMM antibodies (Campellone *et al.*, 2008; Shen *et al.*, 2012) were not amenable to immunohistofluorescence applications, as WHAMM staining was indistinguishable from background fluorescence of the processed kidney tissue.

### Kidney Tissue Preparation

Kidneys were harvested from 25-wk-old mice after cervical dislocation and frozen at -80°C. Tissue extracts were prepared by resuspending thawed kidney thirds in tissue lysis buffer (20 mM HEPES pH 7.4, 100 mM NaCl, 1% IGEPAL CA-630, 1 mM EDTA, 1 mM $Na_3VO_4$, 1 mM NaF, plus 1 mM phenylmethylsulfonyl fluoride, and 10 µg/ml each of aprotinin, leupeptin, pepstatin, and chymostatin) and sonicating at 60% power for 35 s three times using a Fisher dismembranator. The lysates were then clarified by centrifugation at 21,000 × *g* for 12min at 4°C, and the supernatants were collected and centrifuged again at 21,000 × *g* for 6min at 4°C. Extract concentrations were measured using Bradford assays (Bio-Rad), aliquoted, and stored at –80°C.

### Cell Culture

To isolate MEFs, timed matings between WHAMM$^{HET}$ mice were performed and embryos collected at E13.5 in Dulbecco's Modified Eagle Medium (DMEM) containing L-glutamine. Embryos were shipped on ice overnight and within 24 h of harvesting, the livers, hearts, and brains were removed, and the remaining tissues were manually dissociated with scalpels. Embryonic slurries were each transferred into 3 ml of 0.25% Trypsin-EDTA and incubated on ice for 18 h. Without disturbing the settled tissue, 2 ml of the supernatants were removed, and the remaining materials were incubated at 37°C for 30 min. Each cell suspension was mixed with 9 ml of complete media (DMEM containing 10% fetal bovine serum [FBS], GlutaMax, and antibiotic–antimycotic [Life Technologies]) and allowed to adhere to a 10-cm dish at 37°C in 5% $CO_2$ for 24 h. Adherent cells were washed with PBS, collected in 0.05% Trypsin-EDTA, resuspended in media, and split into two new 10-cm dishes. After an additional 24 h of growth, the cells in one dish were washed with PBS, collected in PBS containing 2 mM EDTA, pelleted, resuspended in FBS containing 10% DMSO, aliquoted, and stored in liquid nitrogen. The cells in the second dish were maintained at 35–95% confluence, passaged every 2–3 d, and cryopreserved after passage seven. Upon reanimation, cells went through crisis after three to five more passages, and immortalized cultures eventually emerged. Experiments were conducted after passage 16. Human male HK-2 proximal tubule kidney cells (ATCC) were cultured in DMEM, 10% FBS, GlutaMax, and antibiotic–antimycotic. Experiments were performed using cells that had been in active culture for two to 10 trypsinized passages after thawing.

### Cell Genotyping

MEFs grown in 6-cm dishes were collected in PBS containing 1 mM EDTA, centrifuged, washed with PBS, and recentrifuged. Genomic DNA was isolated from ~$2 \times 10^6$ cells using the Monarch DNA purification Kit (New England Biolabs). For genotyping, PCRs were performed using 50 ng of genomic DNA, gene-specific primers, and Taq polymerase (New England Biolabs). Primers (Supplemental Table S1) were designed to amplify the wild type and knockout alleles as described above, 480 bp and 660 bp fragments of the *Xlr* gene on the X chromosome, a 280 bp fragment of the *Sly* gene on the Y chromosome, and a 241 bp *Gapdh* control. PCR products were subjected to ethidium bromide agarose gel electrophoresis and visualized using ImageJ (Schindelin *et al.*, 2012). Female wild type (WHAMM$^{WT}{}_{X/X}$), female homozygous *Whamm* knockout (WHAMM$^{KO}{}_{X/X}$), male heterozygous (WHAMM$^{HET}{}_{X/Y}$), and male homozygous *Whamm* knockout (WHAMM$^{KO}{}_{X/Y}$) cell populations were generated, but we were unable to isolate male wild type MEFs despite multiple attempts.

### Immunoblotting

Cells grown in 6-well plates were collected in PBS containing 1 mM EDTA and centrifuged before storing at -20°C. Pellets were resuspended in cell lysis buffer (20 mM HEPES pH 7.4, 50 mM NaCl, 0.5 mM EDTA, 1% Triton X-100, 1 mM $Na_3VO_4$, and 1 mM NaF, plus protease inhibitors). Kidney or cell extracts were diluted in SDS–PAGE sample buffer, boiled, centrifuged, and subjected to SDS–PAGE before transfer to nitrocellulose (GE Healthcare). Membranes were blocked in PBS containing 5% milk (PBS-M) before being probed with primary antibodies (Supplemental Table S2) diluted in PBS-M overnight at 4°C plus an additional 2–3 h at room temperature. Membranes were rinsed twice with PBS and washed thrice with PBS + 0.5% Tween-20 (PBS-T). Membranes were then probed with secondary antibodies conjugated to IRDye-800, IRDye-680, or horseradish peroxidase (Supplemental Table S2), rinsed with PBS, and washed with PBS-T. Blots were visualized using a LI-COR Odyssey Fc imaging system, band intensities determined using the Analysis tool in Image Studio software, and quantities of proteins-of-interest normalized to tubulin, actin, and/or GAPDH loading controls.

### Chemical Treatments and Transfections

Cells were seeded onto 12-mm glass coverslips in 24-well plates, allowed to grow for 24 h, and then treated before fixation. MEFs were treated with media containing 50 µM chloroquine (Sigma) or 10 µM rapamycin (Tocris) for 16 h before fixation. HK-2 cells were treated with media containing 50 µM chloroquine, 200 µM CK666 (Calbiochem), or both for 6 h before fixation, or with media containing 5 µg/ml puromycin (Sigma), or puromycin plus 200 µM CK666 for 2 h before fixation. For RNAi experiments, cells were grown in 6-well plates for 24 h, transfected with 40 nM siRNAs (Supplemental Table S1) using RNAiMAX (Invitrogen), incubated in growth media for 24 h, reseeded onto 12-mm glass coverslips, and incubated for an additional 48 h before fixation. For transgene expression, HK-2 cells grown on 12-mm glass coverslips were transfected with 50–100 ng of LAP-WHAMM(WT) or LAP-WHAMM(W807A) (Supplemental Table S1) using LipofectamineLTX with Plus reagent (Invitrogen) diluted in DMEM. After 5 h, cells were incubated in growth media for an additional 18 h before fixation. The LAP tag consists of an N-terminal His-EGFP-TEV-S peptide (Campellone *et al.*, 2008).

### Immunofluorescence Microscopy

Cells grown on coverslips were fixed using 2.5% paraformaldehyde (PFA) in PBS for 30 min, washed, permeabilized with 0.1% TritonX-100 in PBS, washed, and incubated in blocking buffer (PBS containing 1% FBS, 1% BSA, and 0.02% $NaN_3$) for 15 min. For LC3 and GABARAP staining, a methanol denaturation step was included between the PFA and TritonX-100 steps. Cells were probed with primary antibodies (Supplemental Table S2) for 45 min, washed, and treated with AlexaFluor-conjugated secondary antibodies, DAPI, and/or AlexaFluor-conjugated phalloidin (Supplemental Table S2) for 45 min, followed by washes and mounting in ProLong Gold. All tissue and cell images were captured using a Nikon Eclipse T*i* inverted microscope equipped with Plan Apo 100X/1.45, Plan Apo 60X/1.40, or Plan Fluor 20x/0.5 numerical aperture objectives, an Andor Clara-E camera, and a computer running NIS Elements software. Cells were viewed in multiple focal planes, and Z-series were captured in 0.2 µm steps. Images presented in the figures represent either four to five slice projections for tissue samples or one to three slice projections for cell samples.

### Image Processing and Quantification

Images were processed and analyzed using ImageJ (Schindelin *et al.*, 2012). For analyses of Megalin, ACE2, and actin fluorescence intensities per tubule, the Selection tool was used to outline proximal tubule cell clusters, the Measure tool was used to acquire their mean fluorescence intensities, and the background signals from outside of the tubules were subtracted from the mean fluorescence values. To calculate the ACE2 polarity ratios, the Selection tool was used to select ~12 µm$^2$ areas in the apical and cytoplasmic regions of the cluster of proximal tubule cells, the Measure tool was used to acquire the mean fluorescence intensity in each region, background fluorescence was subtracted from these values, and the ACE2 polarity ratio was determined by dividing the apical by cytoplasmic fluorescence per tubule. To generate pixel intensity plots of Megalin or ACE2 with actin and WGA, a 10-µm line was drawn through a cluster

of proximal tubule cells such that the lumen-facing apical region was at the midpoint, and the Plot Profile tool was used to measure the intensity along the line. The background signal from outside of the tubule was subtracted from the mean fluorescence values, and the maximum intensity for each wild type profile was set to one.

For analyses of LC3/GABARAP morphology and actin localization in MEFs and HK-2s, a 3–6 μm line was drawn through a fluorescent autophagic structure, such that the center of the circle or punctum was at the midpoint, and the Plot Profile tool was used to measure the intensity along the line. To determine the fluorescence intensities of LC3 and GABARAP, the Selection tool was used to outline individual cells, and the Measure tool was used to acquire total fluorescence. The number of GABARAP puncta per cell was counted manually. To calculate the puncta-to-cytoplasmic ratio of GABARAP fluorescence, the Selection tool was used to select GABARAP puncta or an equivalently-sized area of the cytoplasm, the Measure tool was used to acquire the mean fluorescence intensity in each area, and the puncta-to-cytoplasmic GABARAP fluorescence ratio was determined. The percentage of cells with LC3-positive rings and the number of LC3-positive rings per cell were counted manually. The percentage of cells with STX17-positive vesicles and the number of STX17-positive vesicles per cell were counted manually. Vesicles were confirmed to be autophagic based on LC3 staining.

### Reproducibility and Statistics

For urinalyses, quantifications were based on data from four to 10 mice of a given genotype. For kidney tissue immunoblotting and immunostaining, quantifications were based on data from kidneys from three to five mice per genotype. For cell-based assays, conclusions were based on observations made from at least three separate experiments, and quantifications were based on data from three representative experiments. The sample size used for statistical tests was the number of mice or the number of times an experiment was performed. Statistical analyses were performed using GraphPad Prism software. Statistics for data sets comparing two conditions were determined using unpaired *t* tests as noted in the Legends. Statistics for data sets with three or more conditions were performed using ANOVAs followed by Tukey's posthoc test unless otherwise indicated. *P* values < 0.05 were considered statistically significant.

## ACKNOWLEDGMENTS

We gratefully acknowledge the contributions of Dorothy Ahlf Wheatcraft and the Protein Sciences and Histopathology Sciences services at The Jackson Laboratory for expert assistance with the work described in this publication. We also thank Naydu Nunno for help processing kidney samples, Adam Zweifach for technical assistance, and Campellone Lab members for their comments on this manuscript. K.G.C. was supported by National Institutes of Health grants GM107441 and AG050774 (www.nih.gov). R.K. was supported by National Institutes of Health grants ES29916, AG038070, DK131019, and DK131061, and the Alport Syndrome Foundation. The funders had no role in study design, data collection and analysis, decision to publish, or preparation of the manuscript.

## REFERENCES

Alekhina O, Burstein E, Billadeau DD (2017). Cellular functions of WASP family proteins at a glance. J Cell Sci 130, 2235–2241.

Arrondel C, Missoury S, Snoek R, Patat J, Menara G, Collinet B, Liger D, Durand D, Gribouval O, Boyer O, *et al.* (2019). Defects in t(6)A tRNA modification due to GON7 and YRDC mutations lead to Galloway-Mowat syndrome. Nat Commun 10, 3967.

Axe EL, Walker SA, Manifava M, Chandra P, Roderick HL, Habermann A, Griffiths G, Ktistakis NT (2008). Autophagosome formation from membrane compartments enriched in phosphatidylinositol 3-phosphate and dynamically connected to the endoplasmic reticulum. J Cell Biol 182, 685–701.

Ballabio A, Bonifacino JS (2020). Lysosomes as dynamic regulators of cell and organismal homeostasis. Nat Rev Mol Cell Biol 21, 101–118.

Ben-Omran T, Fahiminiya S, Sorfazlian N, Almuriekhi M, Nawaz Z, Nadaf J, Khadija KA, Zaineddin S, Kamel H, Majewski J, *et al.* (2015). Nonsense mutation in the WDR73 gene is associated with Galloway-Mowat syndrome. J Med Genet 52, 381–390.

Berquez M, Gadsby JR, Festa BP, Butler R, Jackson SP, Berno V, Luciani A, Devuyst O, Gallop JL (2020). The phosphoinositide 3-kinase inhibitor alpelisib restores actin organization and improves proximal tubule dysfunction in vitro and in a mouse model of Lowe syndrome and Dent disease. Kidney Int 98, 883–896.

Bockenhauer D, Bokenkamp A, van't Hoff W, Levtchenko E, Kist-van Holthe JE, Tasic V, Ludwig M (2008). Renal phenotype in Lowe Syndrome: a selective proximal tubular dysfunction. Clin J Am Soc Nephrol 3, 1430–1436.

Braun DA, Rao J, Mollet G, Schapiro D, Daugeron MC, Tan W, Gribouval O, Boyer O, Revy P, Jobst-Schwan T, *et al.* (2017). Mutations in KEOPS-complex genes cause nephrotic syndrome with primary microcephaly. Nat Genet 49, 1529–1538.

Braun DA, Shril S, Sinha A, Schneider R, Tan W, Ashraf S, Hermle T, Jobst-Schwan T, Widmeier E, Majmundar AJ, *et al.* (2018). Mutations in WDR4 as a new cause of Galloway-Mowat syndrome. Am J Med Genet A 176, 2460–2465.

Campellone KG, Lebek NM, King VL (2023). Branching out in different directions: Emerging cellular functions for the Arp2/3 complex and WASP-family actin nucleation factors. Eur J Cell Biol 102, 151301.

Campellone KG, Webb NJ, Znameroski EA, Welch MD (2008). WHAMM is an Arp2/3 complex activator that binds microtubules and functions in ER to Golgi transport. Cell 134, 148–161.

Campellone KG, Welch MD (2010). A nucleator arms race: cellular control of actin assembly. Nat Rev Mol Cell Biol 11, 237–251.

Colin E, Huynh Cong E, Mollet G, Guichet A, Gribouval O, Arrondel C, Boyer O, Daniel L, Gubler MC, Ekinci Z, *et al.* (2014). Loss-of-function mutations in WDR73 are responsible for microcephaly and steroid-resistant nephrotic syndrome: Galloway-Mowat syndrome. Am J Hum Genet 95, 637–648.

Courtland JL, Bradshaw TW, Waitt G, Soderblom EJ, Ho T, Rajab A, Vancini R, Kim IH, Soderling SH (2021). Genetic disruption of WASHC4 drives endo-lysosomal dysfunction and cognitive-movement impairments in mice and humans. eLife 10, e61590.

Coutts AS, La Thangue NB (2015). Actin nucleation by WH2 domains at the autophagosome. Nat Commun 6, 7888.

Cybulsky AV (2017). Endoplasmic reticulum stress, the unfolded protein response and autophagy in kidney diseases. Nat Rev Nephrol 13, 681–696.

Dai A, Yu L, Wang HW (2019). WHAMM initiates autolysosome tubulation by promoting actin polymerization on autolysosomes. Nat Commun 10, 3699.

Daste F, Walrant A, Holst MR, Gadsby JR, Mason J, Lee JE, Brook D, Mettlen M, Larsson E, Lee SF, *et al.* (2017). Control of actin polymerization via the coincidence of phosphoinositides and high membrane curvature. J Cell Biol 216, 3745–3765.

De Leo MG, Staiano L, Vicinanza M, Luciani A, Carissimo A, Mutarelli M, Di Campli A, Polishchuk E, Di Tullio G, Morra V, *et al.* (2016). Autophagosome-lysosome fusion triggers a lysosomal response mediated by TLR9 and controlled by OCRL. Nat Cell Biol 18, 839–850.

De Matteis MA, Staiano L, Emma F, Devuyst O (2017). The 5-phosphatase OCRL in Lowe syndrome and Dent disease 2. Nat Rev Nephrol 13, 455–470.

Derry JM, Ochs HD, Francke U (1994). Isolation of a novel gene mutated in Wiskott-Aldrich syndrome. Cell 78, 635–644.

Devereaux K, Dall'Armi C, Alcazar-Roman A, Ogasawara Y, Zhou X, Wang F, Yamamoto A, De Camilli P, Di Paolo G (2013). Regulation of mammalian autophagy by class II and III PI 3-kinases through PI3P synthesis. PLoS One 8, e76405.

El Younsi M, Kraoua L, Meddeb R, Ferjani M, Trabelsi M, Ouertani I, Maazoul F, Abid N, Gargah T, M'Rad R. (2019). WDR73-related galloway mowat syndrome with collapsing glomerulopathy. Eur J Med Genet 62, 103550.

Festa BP, Berquez M, Gassama A, Amrein I, Ismail HM, Samardzija M, Staiano L, Luciani A, Grimm C, Nussbaum RL, *et al.* (2019). OCRL deficiency impairs endolysosomal function in a humanized mouse model for Lowe syndrome and Dent disease. Hum Mol Genet 28, 1931–1946.

Gautreau AM, Fregoso FE, Simanov G, Dominguez R (2022). Nucleation, stabilization, and disassembly of branched actin networks. Trends Cell Biol 32, 421–432.
Gomez TS, Gorman JA, de Narvajas AA, Koenig AO, Billadeau DD (2012). Trafficking defects in WASH-knockout fibroblasts originate from collapsed endosomal and lysosomal networks. Mol Biol Cell 23, 3215–3228.
Grieco G, Janssens V, Gaide Chevronnay HP, N'Kuli F, Van Der Smissen P, Wang T, Shan J, Vainio S, Bilanges B, Jouret F, *et al.* (2018). Vps34/PI3KC3 deletion in kidney proximal tubules impairs apical trafficking and blocks autophagic flux, causing a Fanconi-like syndrome and renal insufficiency. Sci Rep 8, 14133.
Harris AN, Lee HW, Osis G, Fang L, Webster KL, Verlander JW, Weiner ID (2018). Differences in renal ammonia metabolism in male and female kidney. Am J Physiol Renal Physiol 315, F211–F222.
Hoopes RR Jr., Shrimpton AE, Knohl SJ, Hueber P, Hoppe B, Matyus J, Simckes A, Tasic V, Toenshoff B, Suchy SF, *et al.* (2005). Dent Disease with mutations in OCRL1. Am J Hum Genet 76, 260–267.
Hu R, McDonough AA, Layton AT (2020). Sex differences in solute transport along the nephrons: effects of Na(+) transport inhibition. Am J Physiol Renal Physiol 319, F487–F505.
Hu X, Mullins RD (2019). LC3 and STRAP regulate actin filament assembly by JMY during autophagosome formation. J Cell Biol 218, 251–266.
Inoue K, Balkin DM, Liu L, Nandez R, Wu Y, Tian X, Wang T, Nussbaum R, De Camilli P, Ishibe S (2017). Kidney tubular ablation of Ocrl/Inpp5b phenocopies lowe syndrome tubulopathy. J Am Soc Nephrol 28, 1399–1407.
Itakura E, Kishi-Itakura C, Mizushima N (2012). The hairpin-type tail-anchored SNARE syntaxin 17 targets to autophagosomes for fusion with endosomes/lysosomes. Cell 151, 1256–1269.
Ito Y, Carss KJ, Duarte ST, Hartley T, Keren B, Kurian MA, Marey I, Charles P, Mendonca C, Nava C, *et al.* (2018). De novo truncating mutations in WASF1 cause intellectual disability with seizures. Am J Hum Genet 103, 144–153.
Jiang C, Gai N, Zou Y, Zheng Y, Ma R, Wei X, Liang D, Wu L (2017). WDR73 missense mutation causes infantile onset intellectual disability and cerebellar hypoplasia in a consanguineous family. Clin Chim Acta 464, 24–29.
Jinks RN, Puffenberger EG, Baple E, Harding B, Crino P, Fogo AB, Wenger O, Xin B, Koehler AE, McGlincy MH, *et al.* (2015). Recessive nephrocerebellar syndrome on the Galloway-Mowat syndrome spectrum is caused by homozygous protein-truncating mutations of WDR73. Brain 138, 2173–2190.
Johansen T, Lamark T (2020). Selective autophagy: ATG8 family proteins, LIR motifs and cargo receptors. J Mol Biol 432, 80–103.
Kabrawala S, Zimmer MD, Campellone KG (2020). WHIMP links the actin nucleation machinery to Src-family kinase signaling during protrusion and motility. PLoS Genet 16, e1008694.
Kast DJ, Zajac AL, Holzbaur EL, Ostap EM, Dominguez R (2015). WHAMM directs the Arp2/3 complex to the ER for autophagosome biogenesis through an actin comet tail mechanism. Curr Biol 25, 1791–1797.
Kerjaschki D, Noronha-Blob L, Sacktor B, Farquhar MG (1984). Microdomains of distinctive glycoprotein composition in the kidney proximal tubule brush border. J Cell Biol 98, 1505–1513.
King VL, Campellone KG (2023). F-actin-rich territories coordinate apoptosome assembly and caspase activation during DNA damage-induced intrinsic apoptosis. Mol Biol Cell 34, ar41.
King VL, Leclair NK, Coulter AM, Campellone KG (2021). The actin nucleation factors JMY and WHAMM enable a rapid Arp2/3 complex-mediated intrinsic pathway of apoptosis. PLoS Genet 17, e1009512.
Klionsky DJ, Abdel-Aziz AK, Abdelfatah S, Abdellatif M, Abdoli A, Abel S, Abeliovich H, Abildgaard MH, Abudu YP, Acevedo-Arozena A, *et al.* (2021). Guidelines for the use and interpretation of assays for monitoring autophagy (4th edition)(1). Autophagy 17, 1–382.
Klootwijk ED, Reichold M, Unwin RJ, Kleta R, Warth R, Bockenhauer D. (2015). Renal Fanconi syndrome: Taking a proximal look at the nephron. Nephrol Dial Transplant 30, 1456–1460.
Koyama-Honda I, Mizushima N (2022). Transient visit of STX17 (syntaxin 17) to autophagosomes. Autophagy 18, 1213–1215.
Kramer DA, Piper HK, Chen B. (2022). WASP family proteins: Molecular mechanisms and implications in human disease. Eur J Cell Biol 101, 151244.
Kumaran GK, Hanukoglu I (2020). Identification and classification of epithelial cells in nephron segments by actin cytoskeleton patterns. FEBS J 287, 1176–1194.
Lamark T, Johansen T (2021). Mechanisms of selective autophagy. Annu Rev Cell Dev Biol 37, 143–169.
Lappalainen P, Kotila T, Jegou A, Romet-Lemonne G (2022). Biochemical and mechanical regulation of actin dynamics. Nat Rev Mol Cell Biol 23, 836–852.
Lazarou M, Sliter DA, Kane LA, Sarraf SA, Wang C, Burman JL, Sideris DP, Fogel AI, Youle RJ. (2015). The ubiquitin kinase PINK1 recruits autophagy receptors to induce mitophagy. Nature 524, 309–314.
Lemaire M (2021). Novel Fanconi renotubular syndromes provide insights in proximal tubule pathophysiology. Am J Physiol Renal Physiol 320, F145–F160.
Levine B, Kroemer G (2019). Biological functions of autophagy genes: A disease perspective. Cell 176, 11–42.
Li H, Liu F, Kuang H, Teng H, Chen S, Zeng S, Zhou Q, Li Z, Liang D, Li Z, *et al.* (2022). WDR73 depletion destabilizes PIP4K2C activity and impairs focal adhesion formation in galloway-mowat syndrome. Biology (Basel) 11, 1397.
Li Q, McDonough AA, Layton HE, Layton AT (2018). Functional implications of sexual dimorphism of transporter patterns along the rat proximal tubule: modeling and analysis. Am J Physiol Renal Physiol 315, F692–F700.
Mann N, Mzoughi S, Schneider R, Kuhl SJ, Schanze D, Klambt V, Lovric S, Mao Y, Shi S, Tan W, *et al.* (2021). Mutations in PRDM15 are a novel cause of Galloway-Mowat syndrome. J Am Soc Nephrol 32, 580–596.
Mathiowetz AJ, Baple E, Russo AJ, Coulter AM, Carrano E, Brown JD, Jinks RN, Crosby AH, Campellone KG (2017). An Amish founder mutation disrupts a PI(3)P-WHAMM-Arp2/3 complex-driven autophagosomal remodeling pathway. Mol Biol Cell 28, 2492–2507.
Mehta ZB, Pietka G, Lowe M (2014). The cellular and physiological functions of the Lowe syndrome protein OCRL1. Traffic 15, 471–487.
Mi N, Chen Y, Wang S, Chen M, Zhao M, Yang G, Ma M, Su Q, Luo S, Shi J, *et al.* (2015). CapZ regulates autophagosomal membrane shaping by promoting actin assembly inside the isolation membrane. Nat Cell Biol 17, 1112–1123.
Mizushima N (2020). The ATG conjugation systems in autophagy. Curr Opin Cell Biol 63, 1–10.
Nakamura S, Yoshimori T. (2017). New insights into autophagosome-lysosome fusion. J Cell Sci 130, 1209–1216.
Nguyen TN, Padman BS, Usher J, Oorschot V, Ramm G, Lazarou M (2016). Atg8 family LC3/GABARAP proteins are crucial for autophagosome-lysosome fusion but not autophagosome formation during PINK1/Parkin mitophagy and starvation. J Cell Biol 215, 857–874.
Norden AGW, Lapsley M, Igarashi T, Kelleher CL, Lee PJ, Matsuyama T, Scheinman SJ, Shiraga H, Sundin DP, Thakker RV, *et al.* (2002). Urinary megalin deficiency implicates abnormal tubular endocytic function in Fanconi syndrome. J Am Soc Nephrol 13, 125–133.
Oltrabella F, Pietka G, Ramirez IB, Mironov A, Starborg T, Drummond IA, Hinchliffe KA, Lowe M (2015). The Lowe syndrome protein OCRL1 is required for endocytosis in the zebrafish pronephric tubule. PLoS Genet 11, e1005058.
Pankiv S, Clausen TH, Lamark T, Brech A, Bruun JA, Outzen H, Overvatn A, Bjorkoy G, Johansen T (2007). p62/SQSTM1 binds directly to Atg8/LC3 to facilitate degradation of ubiquitinated protein aggregates by autophagy. J Biol Chem 282, 24131–24145.
Pollard TD (2016). Actin and actin-binding proteins. Cold Spring Harb Perspect Biol 8, a018226.
Ransick A, Lindstrom NO, Liu J, Zhu Q, Guo JJ, Alvarado GF, Kim AD, Black HG, Kim J, McMahon AP (2019). Single-cell profiling reveals sex, lineage, and regional diversity in the mouse kidney. Dev Cell 51, 399–413 e397.
Rinschen MM, Harder JL, Carter-Timofte ME, Zanon Rodriguez L, Mirabelli C, Demir F, Kurmasheva N, Ramakrishnan SK, Kunke M, Tan Y, *et al.* (2022). VPS34-dependent control of apical membrane function of proximal tubule cells and nutrient recovery by the kidney. Sci Signal 15, eabo7940.
Rivers E, Thrasher AJ (2017). Wiskott-Aldrich syndrome protein: Emerging mechanisms in immunity. Eur J Immunol 47, 1857–1866.
Ropers F, Derivery E, Hu H, Garshasbi M, Karbasiyan M, Herold M, Nurnberg G, Ullmann R, Gautreau A, Sperling K, *et al.* (2011). Identification of a novel candidate gene for nonsyndromic autosomal recessive intellectual disability: the WASH complex member SWIP. Hum Mol Genet 20, 2585–2590.
Rosti RO, Sotak BN, Bielas SL, Bhat G, Silhavy JL, Aslanger AD, Altunoglu U, Bilge I, Tasdemir M, Yzaguirrem AD, *et al.* (2017). Homozygous mutation in NUP107 leads to microcephaly with steroid-resistant

nephrotic condition similar to Galloway-Mowat syndrome. J Med Genet 54, 399–403.
Rottner K, Faix J, Bogdan S, Linder S, Kerkhoff E (2017). Actin assembly mechanisms at a glance. J Cell Sci 130, 3427–3435.
Russo AJ, Mathiowetz AJ, Hong S, Welch MD, Campellone KG (2016). Rab1 recruits WHAMM during membrane remodeling but limits actin nucleation. Mol Biol Cell 27, 967–978.
Sarraf SA, Shah HV, Kanfer G, Pickrell AM, Holtzclaw LA, Ward ME, Youle RJ. (2020). Loss of TAX1BP1-directed autophagy results in protein aggregate accumulation in the brain. Mol Cell 80, 779–795.e710.
Schell C, Baumhakl L, Salou S, Conzelmann AC, Meyer C, Helmstadter M, Wrede C, Grahammer F, Eimer S, Kerjaschki D, *et al.* (2013). N-wasp is required for stabilization of podocyte foot processes. J Am Soc Nephrol 24, 713–721.
Schell C, Sabass B, Helmstaedter M, Geist F, Abed A, Yasuda-Yamahara M, Sigle A, Maier JI, Grahammer F, Siegerist F, *et al.* (2018). ARP3 controls the podocyte architecture at the kidney filtration barrier. Dev Cell 47, 741–757.e748.
Schindelin J, Arganda-Carreras I, Frise E, Kaynig V, Longair M, Pietzsch T, Preibisch S, Rueden C, Saalfeld S, Schmid B, *et al.* (2012). Fiji: an open-source platform for biological-image analysis. Nat Methods 9, 676–682.
Schluter K, Waschbusch D, Anft M, Hugging D, Kind S, Hanisch J, Lakisic G, Gautreau A, Barnekow A, Stradal TE (2014). JMY is involved in anterograde vesicle trafficking from the trans-Golgi network. Eur J Cell Biol 93, 194–204.
Shang D, Wang L, Klionsky DJ, Cheng H, Zhou R (2021). Sex differences in autophagy-mediated diseases: toward precision medicine. Autophagy 17, 1065–1076.
Shen QT, Hsiue PP, Sindelar CV, Welch MD, Campellone KG, Wang HW (2012). Structural insights into WHAMM-mediated cytoskeletal coordination during membrane remodeling. J Cell Biol 199, 111–124.
Shikama N, Lee CW, France S, Delavaine L, Lyon J, Krstic-Demonacos M, La Thangue NB (1999). A novel cofactor for p300 that regulates the p53 response. Mol Cell 4, 365–376.
Snapper SB, Takeshima F, Anton I, Liu CH, Thomas SM, Nguyen D, Dudley D, Fraser H, Purich D, Lopez-Ilasaca M, *et al.* (2001). N-WASP deficiency reveals distinct pathways for cell surface projections and microbial actin-based motility. Nat Cell Biol 3, 897–904.
Song J, Yu J, Prayogo GW, Cao W, Wu Y, Jia Z, Zhang A (2019). Understanding kidney injury molecule 1: A novel immune factor in kidney pathophysiology. Am J Transl Res 11, 1219–1229.
Spence EF, Soderling SH (2015). Actin out: Regulation of the synaptic cytoskeleton. J Biol Chem 290, 28613–28622.
Srivastava S, Macke EL, Swanson LC, Coulter D, Klee EW, Mullegama SV, Xie Y, Lanpher BC, Bedoukian EC, Skraban CM, *et al.* (2021). Expansion of the genotypic and phenotypic spectrum of WASF1-related neurodevelopmental disorder. Brain Sci 11, 931.
Suchy SF, Nussbaum RL (2002). The deficiency of PIP2 5-phosphatase in Lowe syndrome affects actin polymerization. Am J Hum Genet 71, 1420–1427.
Tang C, Livingston MJ, Liu Z, Dong Z. (2020). Autophagy in kidney homeostasis and disease. Nat Rev Nephrol 16, 489–508.
Tilley FC, Arrondel C, Chhuon C, Boisson M, Cagnard N, Parisot M, Menara G, Lefort N, Guerrera IC, Bole-Feysot C, *et al.* (2021). Disruption of pathways regulated by integrator complex in Galloway-Mowat syndrome due to WDR73 mutations. Sci Rep 11, 5388.
Torres-Pinzon DL, Ralph DL, Veiras LC, McDonough AA (2021). Sex-specific adaptations to high-salt diet preserve electrolyte homeostasis with distinct sodium transporter profiles. Am J Physiol Cell Physiol 321, C897–C909.
Tsuboyama K, Koyama-Honda I, Sakamaki Y, Koike M, Morishita H, Mizushima N (2016). The ATG conjugation systems are important for degradation of the inner autophagosomal membrane. Science 354, 1036–1041.
Utsch B, Bokenkamp A, Benz MR, Besbas N, Dotsch J, Franke I, Frund S, Gok F, Hoppe B, Karle S, *et al.* (2006). Novel OCRL1 mutations in patients with the phenotype of Dent disease. Am J Kidney Dis 48, 942 e1–14.
Valdmanis PN, Meijer IA, Reynolds A, Lei A, MacLeod P, Schlesinger D, Zatz M, Reid E, Dion PA, Drapeau P, *et al.* (2007). Mutations in the KIAA0196 gene at the SPG8 locus cause hereditary spastic paraplegia. Am J Hum Genet 80, 152–161.
van der Wijst J, Belge H, Bindels RJM, Devuyst O (2019). Learning physiology from inherited kidney disorders. Physiol Rev 99, 1575–1653.
Vargas JNS, Hamasaki M, Kawabata T, Youle RJ, Yoshimori T. (2023). The mechanisms and roles of selective autophagy in mammals. Nat Rev Mol Cell Biol 24, 167–185.
Vartiainen MK, Machesky LM (2004). The WASP-Arp2/3 pathway: Genetic insights. Curr Opin Cell Biol 16, 174–181.
Veiras LC, Girardi ACC, Curry J, Pei L, Ralph DL, Tran A, Castelo-Branco RC, Pastor-Soler N, Arranz CT, Yu ASL, *et al.* (2017). Sexual dimorphic pattern of renal transporters and electrolyte homeostasis. J Am Soc Nephrol 28, 3504–3517.
Vicinanza M, Di Campli A, Polishchuk E, Santoro M, Di Tullio G, Godi A, Levtchenko E, De Leo MG, Polishchuk R, Sandoval L, *et al.* (2011). OCRL controls trafficking through early endosomes via PtdIns4,5P(2)-dependent regulation of endosomal actin. EMBO J 30, 4970–4985.
Vodopiutz J, Seidl R, Prayer D, Khan MI, Mayr JA, Streubel B, Steiss JO, Hahn A, Csaicsich D, Castro C, *et al.* (2015). WDR73 mutations cause infantile neurodegeneration and variable glomerular kidney disease. Hum Mutat 36, 1021–1028.
Warner FJ, Lew RA, Smith AI, Lambert DW, Hooper NM, Turner AJ (2005). Angiotensin-converting enzyme 2 (ACE2), but not ACE, is preferentially localized to the apical surface of polarized kidney cells. J Biol Chem 280, 39353–39362.
Wu K, Seylani A, Wu J, Wu X, Bleck CKE, Sack MN (2021). BLOC1S1/GCN5L1/BORCS1 is a critical mediator for the initiation of autolysosomal tubulation. Autophagy 17, 1–18.
Xia P, Wang S, Du Y, Zhao Z, Shi L, Sun L, Huang G, Ye B, Li C, Dai Z, *et al.* (2013). WASH inhibits autophagy through suppression of Beclin 1 ubiquitination. EMBO J 32, 2685–2696.
Yan C, Martinez-Quiles N, Eden S, Shibata T, Takeshima F, Shinkura R, Fujiwara Y, Bronson R, Snapper SB, Kirschner MW, *et al.* (2003). WAVE2 deficiency reveals distinct roles in embryogenesis and Rac-mediated actin-based motility. EMBO J 22, 3602–3612.
Zhang X, Jefferson AB, Auethavekiat V, Majerus PW (1995). The protein deficient in Lowe syndrome is a phosphatidylinositol-4,5-bisphosphate 5-phosphatase. Proc Natl Acad Sci USA 92, 4853–4856.
Zhao YG, Zhang H (2019). Autophagosome maturation: An epic journey from the ER to lysosomes. J Cell Biol 218, 757–770.
Zuchero JB, Coutts AS, Quinlan ME, Thangue NB, Mullins RD (2009). p53-cofactor JMY is a multifunctional actin nucleation factor. Nat Cell Biol 11, 451–459.